The impact of Radial and Non-Radial IMF on the Earth's Magnetopause Size and Shape, and Dawn-Dusk Asymmetry from Global 3D Kinetic Simulations

Suleiman Baraka[1,1,1], Olivier Le Contel Le Contel[2,2,2], Lotfi Ben-Jaffel[3,3,3], and Bill Moore[1,1,1]

[1]National Institute of Aerospace
[2]CNRS/Ecole Polytechnique/Sorbonne Université/Université Paris-Saclay/Obser. de Paris
[3]Institut d'Astrophysique de Plasma

November 30, 2022

Abstract

The boundary between the solar wind (SW) and the Earths magnetosphere, the magnetopause (MP), is highly dynamic. Its location and shape depend on SW dynamic pressure and interplanetary magnetic field (IMF) orientation. We use a 3D kinetic Particle-In-Cell code (IAPIC) to simulate an event observed by THEMIS spacecraft on July 16, 2007. We investigate the impact of radial ($\vartheta Bx=0*$) and non-radial ($\vartheta Bx=50*$) IMF on the shape and size of Earths MP for a dipole tilt of 31* using maximum density gradient and pressure balance methods. Using the Shue model as a reference (MP at 10.3 RE), we find that for non-radial IMF the MP expands by 1.4 and 1.7RE along the the Sun-Earth (OX) and tilted magnetic equatorial (Tilt) axes, respectively, and it expands by 0.5 and 1.6RE for radial IMF along the same respective axes. When the effect of backstreaming ions is removed from the bulk flow, the expansion ranges are 1.0 and 1.3RE and 0.2, and 1.2RE, respectively. It is found that the percentage of backstreaming to bulk flow ions are 16.5% and 20% for radial and non-radial IMF. We also show that when the backstreaming ions are not identified, up to 40% of the observed expansion that is due to backstreaming particles can be inadvertently attributed to a change in the SW upstream properties. Finally, we quantified the temperature anisotropy in the magnetosheath, and observe a strong dawn-dusk asymmetry in the MP location, being more extended on the duskside than on the dawnside.

The impact of Radial and Non-Radial IMF on the Earth's Magnetopause Size, Shape, and Dawn-Dusk Asymmetry from Global 3D Kinetic Simulations

Suleiman M Baraka [1,3]**, O. Le Contel** [2]**, L. Ben−Jaffel**[3]**, W. B. Moore**[1,4]

[1]National Institute of Aerospace, 100 Exploration Way, Hampton, VA 23666
[2]Laboratoire de Physique des Plasmas, UMR7648 ,CNRS/Sorbonne Université/Université Paris-Saclay/Observatoire de Paris/Ecole Polytechnique Institut Polytechnique de Paris, Palaiseau, France.
[3]Institut d'Astrophysique de Paris. Sorbonne Universités, UPMC & CNRS, 98 bis Bd. Arago, F-75014 Paris, France
[4]Hampton University, 154 William R. Harvey Way Hampton, VA 23668

Key Points:

- The magnetopause expansion at the subsolar point for radial and non-radial IMF is partly due to the reduction of the solar wind dynamic pressure caused by back-streaming ions.
- Although backstreaming ions constitute only 16.5% and 20% of the solar wind bulk flow for radial and non-radial IMF, they strongly modify the dynamic pressure.
- For both radial and non-radial IMF, the magnetopause is asymmetric, being more extended on the duskside than on the dawnside.

Corresponding author: Suleiman M Baraka, `suleiman.baraka@nianet.org`

Abstract

The boundary between the solar wind (SW) and the Earth's magnetosphere, the magnetopause (MP), is highly dynamic. Its location and shape depend on SW dynamic pressure and interplanetary magnetic field (IMF) orientation. We use a 3D kinetic Particle-In-Cell code (IAPIC) to simulate an event observed by THEMIS spacecraft on July 16, 2007. We investigate the impact of radial (θ_{Bx}=0°) and non-radial (θ_{Bx}=50°) IMF on the shape and size of Earth's MP for a dipole tilt of 31° using maximum density gradient and pressure balance methods. Using the Shue model as a reference (MP at 10.3 R_E), we find that for non-radial IMF the MP expands by 1.4 and 1.7R_E along the the Sun-Earth (OX) and tilted magnetic equatorial (Tilt) axes, respectively, and it expands by 0.5 and 1.6R_E for radial IMF along the same respective axes. When the effect of backstreaming ions is removed from the bulk flow, the expansion ranges are 1.0 and 1.3R_E and 0.2, and 1.2R_E, respectively. It is found that the percentage of backstreaming to bulk flow ions are 16.5% and 20% for radial and non-radial IMF. We also show that when the backstreaming ions are not identified, up to 40% of the observed expansion that is due to backstreaming particles can be inadvertently attributed to a change in the SW upstream properties. Finally, we quantified the temperature anisotropy in the magnetosheath, and observe a strong dawn-dusk asymmetry in the MP location, being more extended on the duskside than on the dawnside.

Plain Language Summary

The Earth's magnetopause (MP) is a sensitive region where the pressure of the Earth magnetic field balances the shocked solar wind ram and thermal pressures. Accurate space weather monitoring and forecast require an in-depth knowledge of this region and of the physical processes that affect it. We investigate the effects of the orientation of the interplanetary magnetic field (IMF) on the MP size, location, and shape by using a numerical technique (3D kinetic simulation) that uses macro-ions and macro-electrons to mimic the real charged species and explicitly resolves their motion. We are able to extract the shape and location of the MP in three dimensions to estimate the sensitivity of the MP position to

⁴⁸ the ambient IMF and solar wind conditions, while our explicit tracking of ion motions allows

⁴⁹ us to investigate the role of ion species backscattered by the Earth's bow shock and magne-

⁵⁰ tosheath. We find that when the IMF has a strong component in the Earth-Sun direction

⁵¹ (radial or non-radial IMF), these backscattered ions play an important role in reducing the

⁵² effective pressure of the incoming solar wind and allowing the MP to expand outward.

1 Introduction

The magnetic fields of planets such as Mercury, Earth, and the giant planets present an obstacle to the supersonic solar wind (SW). As a result, a shock forms and the solar wind is redirected around the obstacle producing a cavity which is called the magnetosphere (e.g., Parks, 1991). The boundary between the shocked SW and the plasma in the magnetosphere is the magnetopause (MP). At the subsolar point, the classical fluid description of the SW stagnation flow derives the location of the magnetopause by the balance between the planetary magnetic field pressure and the dynamic pressure of the SW. Plasma boundary layers form on either side of the magnetopause with the magnetosheath boundary layer (MSBL) on the sunward side and the low-latitude boundary layer (LLBL) on the magnetosphere side. Both layers play an important role in plasma exchange across the magnetopause (e.g., Pi et al., 2018).

The magnetopause structure is significantly influenced by the interplanetary magnetic field (IMF) orientation. While the impact of southward (Yu & Ridley, 2009; Heikkila, 2011; Tan et al., 2011; Suvorova & Dmitriev, 2015; Berchem et al., 2016) and northward IMF (Sorathia et al., 2019; Luo et al., 2013; Bobra et al., 2004; Wang et al., 2018) on the dynamics of Earth's magnetosphere have been extensively studied in the last four decades, only recently has attention been focused on radially-dominant IMF conditions, which will be called radial IMF for the remainder of this paper. For most solar wind plasma conditions at the orbital position of planets, bow shocks are collisionless and supercritical shocks, which by definition, reflect and accelerate a fraction of the plasma impinging on them. These backstreaming particles lead to the formation of the ion foreshock region upstream (e.g., Turner et al., 2018, p. 206).

Following early satellite observations (Greenstadt et al., 1968; Asbridge et al., 1968), the idea of an extended foreshock that diverts the solar wind around the magnetosphere and reduces the solar wind dynamic pressure at the subsolar magnetopause was proposed for radial IMF conditions (Fairfield et al., 1990; Merka et al., 2003; Jelínek et al., 2010;

Suvorova et al., 2010). The distance and shape of the equatorial magnetopause is strongly affected by radial IMF, resulting in a global expansion of the magnetopause (Grygorov et al., 2017). Zhang et al. (2019) found that a dawn-dusk asymmetry exists in the magnetosheath, directly related to the IMF orientation. Evidently, the plasma distribution and the IMF are correlated to these asymmetries which are either generated at the bow shock or inside the magnetosheath itself.

Most magnetopause observations during radial IMF have noticed a large magnetopause expansion that was connected with a significant distortion of the magnetopause surface. Large magnetopause distortion and anomalous sunward magnetosheath flows were reported in one radial IMF event by (Shue et al., 2009). The finding of magnetopause displacement during radial IMF conditions was also documented in a statistical study based on a large set of magnetopause crossings using THEMIS (Dušík et al., 2010) and GOES (Park et al., 2016) data. A systematic increase of observed magnetopause distances for radial IMF was found, ranging from $0.3R_E$ at $90°$ cone angle to $\approx 1.7R_E$ at $0°$ or $180°$ cone angles compared to empirical models. However, Dušík et al. (2010); Suvorova and Dmitriev (2015) pointed out a large dispersion in their statistical results attributed to the difficulty to propagate radial IMF to the magnetopause. In contrast, using THEMIS data and empirical models of the MP, Grygorov et al. (2017) concluded that the distance of the equatorial magnetopause is strongly affected by radial IMF, expanding globally and independent of the local time, upstream value of other solar wind parameters or the tilt of the Earth magnetic dipole.

It is interesting to remark that no self-consistent model exists today in the literature that can explain the observed MP displacement or its asymmetry, particularly with the difficulty MHD approaches have to accurately model reflected SW ions in the foreshock region (Sibeck et al., 2001). In a recent study, (Samsonov et al., 2017) used previous statistical results to suggest that the density and velocity in the foreshock region decrease to $\sim 60\%$ and $\sim 94\%$ of the undisturbed SW values when the cone angle falls below $50°$ causing a drop in the SW dynamic pressure of $\sim 53\%$ that might cause the MP displacement. In a second step,

107 those authors modified the upstream SW parameters in a global MHD model to take these
108 foreshock effects into account, which helped them predict MP distances during non-radial
109 IMF intervals close to those observed by THEMIS. More precisely, using time dependent SW
110 conditions provided by ACE and WIND measurements in their simulations, they applied
111 a $\sim 53\%$ dynamic pressure reduction as soon as the SW cone angle becomes smaller than
112 $50°$. This limit was chosen in order to smooth the swap between radial (reduced dynamic
113 pressure) and non-radial (unchanged dynamic pressure) regimes (Samsonov et al., 2017). In
114 the present study, we employ constant upstream SW conditions. For the sake of covering
115 the full range of cone angles considered in the simulations of (Samsonov et al., 2017), we
116 have performed simulations for the two limit cases of $0°$ (referred to as radial IMF) and
117 $\sim 50°$ cone angle (referred to as non-radial IMF). We note that there is no consistent usage
118 in the literature of the terms radial or non-radial IMF.

119 According to Samsonov et al. (2017), the strong total pressure decrease in data seems to
120 be a local, rather than a global, phenomenon. Those authors conceded that their model was
121 not self-consistent in the sense that the modified upstream SW parameter adjustment was
122 global and not specific to the foreshock region for which the statistical results (discussed
123 above) were initially derived. One of the goals of this study is to investigate the role of
124 backscattered ions in producing decreased SW dynamic pressure ahead of the magnetopause
125 by resolving them in a 3D kinetic simulation.

126 In addition to the expansion of the MP, the other focus of this study is the gener-
127 ation of dawn-dusk asymmetry under radial IMF, which has been investigated for many
128 decades (Akasofu et al., 1982; Akasofu, 1991; Haaland et al., 2017, and references therein).
129 Dawn-dusk asymmetries are ubiquitous features of the coupled solar wind-magnetosphere-
130 ionosphere system. During the last decades,the increasing availability of satellite and
131 ground-based measurements has made it possible to study these phenomena in more de-
132 tail (e.g., B. M. Walsh, 2017). Most studies reported so far agree that the dawn-dusk
133 asymmetry is primarily the result of the Parker spiral solar wind impinging with a specific

134 geometric configuration that impacts and preconditions the magnetosphere (e.g., Haaland

135 et al., 2017, and references therein). Under radial conditions, the IMF and the SW flow

136 are symmetric with respect to the Sun-Earth line. Under those conditions, one cannot in-

137 voke the asymmetry due to the Parker spiral shape to explain any dawn-dusk asymmetry.

138 Therefore, other physical processes, like kinetic effects, should be investigated to explain

139 any potential asymmetry. For instance, statistical studies based on THEMIS and Cluster

140 measurements confirm a rather global expansion of the magnetopause under radial IMF

141 without significant dawn-dusk asymmetries was detected (Zhang et al., 2019). The same

142 statistical study showed that magnetic reconnection (MR) is nearly absent during radial

143 IMF, in contrast to the north IMF conditions during which lobe MR and the consequent

144 dawn-dusk asymmetries are strong (Zhang et al., 2019). However, possible influence of ra-

145 dial IMF on the aurora and dayside magnetic reconnection for different dipole tilt angles

146 have also been investigated by (Østgaard et al., 2003; Zhang et al., 2019).

147 Kinetic effects are expected to trigger a large set of distinct dawn-dusk asymmetries up-

148 stream of the magnetosphere due to the formation of the foreshock region that is connected

149 with solar wind particles backscattered at the bow shock and magnetosheath. Although

150 much of the plasma passes through the bow shock, the reflected population generates a

151 number of plasma instabilities, which trigger waves and generate wave-particle interactions

152 as well as other dynamics at the non-parallel shock that should favor dawn-dusk asymme-

153 tries (e.g., B. M. Walsh, 2017, and references therein). The radial IMF condition would

154 thus be the ideal configuration to reveal such kinetic effects and determine their role in

155 producing the dawn-dusk asymmetry so far observed (Zhang et al., 2019). For reference,

156 using Cluster single/multiple spacecraft measurements, Haaland et al. (2014) discussed the

157 dawn-dusk asymmetry at the flanks and at the dayside MP. Similar results were also re-

158 ported by Haaland et al. (2019), as observed by two of the THEMIS spacecraft, showing

159 the magnetopause being thicker on dawn ($\sim 14\lambda_i$, λ_i being the ion inertial length) than

160 on dusk ($\sim 8\lambda_i$), however no radial IMF conditions were included in the statistical study.

161 Additionally, other observations from INTERBALL-1 and MAGION-4 spacecraft revealed

asymmetry and deformation at the turbulent magnetopause (Šafránková et al., 2000). Using Geotail observations for northern and southern IMF, Wang et al. (2006) thoroughly discussed the dawn-dusk asymmetry in ion density and temperature based on equatorial distribution of plasma sheet ions.

To interpret the magnetopause motion and the dawn-dusk asymmetry, many sophisticated models have been utilized, ranging from MHD to hybrid simulations. Early theoretical studies showed a contrast of 10%-20% between dawn and dusk bulk plasma properties (e.g., Němeček et al., 2002; Walsh et al., 2012), however; those MHD-based models do not explicitly resolve kinetic effects, particularly at the foreshock region. For instance, using a global hybrid model (kinetic ions and fluid electrons), Blanco-Cano et al. (2009) studied radial IMF ($\theta_{vB} = 0$) impact on the solar wind interaction with the Earth's magnetosphere. The study focused on the micro-physics processes and wave-particle interactions in the foreshock region but briefly mentioned the dawn-dusk asymmetry issue. Three other models i.e. hybrid, Hall-less and Hall-MHD simulations have been tested in one study by Karimabadi et al. (2004) for the analysis of MR regimes with the conclusion that dawn-dusk asymmetry is obtained and should be related to ions flow. Recently, Turc et al. (2020) used the hybrid -Vlasiator 2D-3V code to study asymmetries in the Earth magnetosheath for different IMF conditions. For reference, the Vlasiator code provides a kinetic description of ions, solving directly the Vlasov equation for the particle distribution function in 2D-3D space, but assumes a fluid description for electrons (e.g., Palmroth et al., 2018). The authors report asymmetries larger than observed for the magnetic field strength, the plasma density, and bulk velocity, a discrepancy that was attributed to using a single set of upstream conditions in their simulations. It is interesting to remark that those authors obtained a stronger asymmetry for magnetic field strength when IMF gets closer to the radial configuration. However, it was not clear how the 2D spatial assumption and the fluid description of electrons in their simulations affected the reported magnetosheath asymmetries.

188 Based on the discussion above, two important questions appear: 1) what happens to

189 the magnetopause shape, size, and location if flow-aligned IMF is applied to the system

190 when kinetic effects are included for all species? and 2) does this generate asymmetry in

191 the dawn-dusk and south-north directions so in the dayside magnetosphere?

192 To answer these questions, we undertake a modeling study utilizing IAPIC, a particles-

193 in-cell code (discussed in section 2). Our strategy is to be able to follow ions and electrons

194 self-consistently with the Maxwell equations describing the fields. Thus the full range of

195 collisionless plasma physics is captured for the macro-ions and macro-electrons involved in

196 IAPIC, yet with limitations due to the grid spatial resolution and assumptions made on the

197 plasma properties (particles density, ion/electron mass ratio, etc.) that we carefully discuss

198 in section 2 (see Blanco-Cano et al., 2006; Eastwood, 2008; Jacobsen et al., 2009; Brackbill,

199 2011; Masters et al., 2013; Ben-Jaffel & Ballester, 2014; S. Baraka, 2016). We adopt the

200 initial and the boundary conditions reported in (Suvorova et al., 2010; Samsonov et al.,

201 2017), we used single physical units for each parameter that were used in CCMC reported

202 in (Samsonov et al., 2017).

203 This paper is structured as follows. This section has introduced the impact of radial

204 IMF orientation on the dynamics of the Earth's magnetosphere and presented a brief survey

205 of observations of asymmetry in planetary magnetospheres. Two IMF orientations, namely,

206 radial IMF ($B = B_x$, 0° cone angle) and non-radial IMF ($|Bz| < |Bx| < |By|$, $\sim 50°$ cone

207 angle) will be covered in the current study.

208 In section 2, we describe the IAPIC code in detail. The scaling of plasma parameters is

209 also presented and tabulated. In section 3, we show our findings regarding the magnetopause

210 motion and the magnetosheath asymmetry, an opportunity to compare to previous modeling

211 results and observations. In section 4, we discuss in detail the impact of the purely and non-

212 radial IMF on the dynamics of the Earth's magnetosphere, in light of the results obtained

213 so far. In section 5, we present a summary of our findings and future related work.

2 Initial conditions and Simulation Model: IAPIC

2.1 Simulation Model: IAPIC

We use the Institut d'Astrophysique de Paris-Particle-In-Cell EM 3D global code (IAPIC) for treating the plasma kinetically. IAPIC has previously been applied to simulate various magnetospheres in the solar system (S. Baraka & Ben-Jaffel, 2011; Ben-Jaffel & Ballester, 2013, 2014; S. Baraka, 2016). IAPIC handles the equations of motion for a large number of macro-particles (macro-ions and macro-electrons) self-consistently under the direct impact of electromagnetic fields through Lorentz force law (S. Baraka & Ben-Jaffel, 2007; Artemyev & Zelenyi, 2012).

The code was originally written by (Buneman et al., 1992), which used the boundary conditions reported in (Lindman, 1975) and charge conserving conditions as described in (Villasenor & Buneman, 1992). We use physical units for each parameter from (Samsonov et al., 2017) and scaled them to IAPIC values using a transformation matrix to convert GSM coordinates to the IAPIC code coordinates (see Fig. 1) as reported in (Cai et al., 2003). The solar wind parameters are tabulated in Table 1 for radial IMF and Table2 for non-radial IMF (see also, Table 1, Cai et al., 2015).

We follow the evolution of the fields and particles within a 61x45x45 R_E domain with Earth centered and 20 R_E downstream of the sunward (inlet) side (Table 1). We chose time step $t = 3700\Delta t$ as our comparison point which corresponds to 24 minutes of real time (approximately twice the SW transit time) after starting the simulation. Each time step is equivalent to ≈ 0.38 sec and the spatial resolution of the code is $0.2R_E$. We track 7.0×10^7 particle pairs, with an ion to electron mass ratio of 64.

Our solar wind parameters for both IMF orientations are given in Tables 1 and 2 for radial and non-radial IMF, respectively. The parameters are set such that a consistent initial conditions are validated before the code run starts, denoted as $t = 0\Delta$, and at the step time,

where the current study is considered i.e. $t = 3700\Delta t$. These two tables are compared to a

similar study by (Cai et al., 2015)

Step time	$t = 0\Delta t$		$t = 3700\Delta t$	
Species/Parameters	ions	electrons	ions	electrons
Thermal velocity, $V_{thi,e}$	0.025	0.1	0.06	0.41
Debye length, $\Delta_{i,e}$	0.8	0.4	1.48	1.35
Larmor radius, $\lambda_{i,e}$	44.95	0.7	11.51	1.31
Gyro-frequency $\omega_{ci,e}$	$3.\times10^{-3}$	0.20	$2.\times10^{-3}$	0.31
Plasma-frequency $\omega_{pi,e}$	0.03	0.25	0.04	0.30
Temperature, $T_{i,e}$	$1.\times10^{-3}$	$2.\times10^{-4}$	4.9×10^{-3}	4.09×10^{-3}
Gyroperiod	2094.4	31.4	1289.81	20.15
Inertial length $d_{i,e}$	16.6	2.0	13.23	1.65

Unitless   values

Step time	$t = 0$	$t = 3700\Delta t$
Sound speed C_s	0.045	0.0.1
Alfvén speed v_A	0.050	0.06
Alfvén Mach number M_A	2.83	1.4
Sonic Mach number M_s	3.16	0.92
Magnetosonic Mach number M_{ms}	2.0	0.77

Loaded Simulation Box Information

grid size	$\Delta = 0.2 R_E = \Delta x = \Delta y = \Delta z$
Time Step	$\Delta t = \Delta_x / \Delta_v = 7.08$
Simulation box size	$(305 \times 225 \times 255)\Delta$
# of pair-particles	7×10^7 ion/electrons pairs
Ion to electron mass ratio	64
Particle density	$n_i = n_e = 4/\Delta^3$

Table 1. Solar wind parameters at the initial state and after t=3700 Δt in the undisturbed solar wind for both ions and electrons for radial IMF.

Step time	$t =0$		$t = 3700\Delta t$	
Species/Parameters	ions	electrons	ions	electrons
Thermal velocity, $V_{thi,e}$	0.025	0.1	0.04	0.39
Debye length, $\Delta_{i,e}$	0.8	0.4	0.87	1.15
Larmor radius, $\lambda_{i,e}$	26.26	0.4	6.85	1.12
Gyro-frequency $\omega_{ci,e}$	$5.\times 10^{-3}$	0.343	0.01	0.35
Plasma-frequency $\omega_{pi,e}$	0.03	0.25	0.04	0.34
Temperature, $T_{i,e}$	9×10^{-4}	$2.\times 10^{-4}$	2.18×10^{-3}	3.75×10^{-3}
Gyroperiod	1256.6	18.3	1153.15	18.02
Inertial length $d_{i,e}$	16.1	2.0	11.71	1.46

Unitless values		
Step time	$\Delta t =0$	$t = 3700\Delta t$
Sound speed C_s	0.045	0.08
Alfvén speed v_A	0.05	0.06
Alfvén Mach number M_A	2.83	1.23
Sonic Mach number M_s	3.16	0.99
Magnetosonic Mach number M_{ms}	2.0	0.77

Loaded Simulation Box Information	
grid size	$\Delta = 0.2R_E = \Delta x = \Delta y = \Delta z$
Time Step	$\Delta t = \Delta_x/\Delta_v = 7.08$
Simulation box size	$(305 \times 225 \times 255)\Delta$
# of pair-particles	7×10^7 ion/electrons pairs
Ion to electron mass ratio	64
Particle density	$n_i = n_e = 4/\Delta^3$

Table 2. Solar wind parameters at the initial state and after t=3700 Δt in the undisturbed solar wind for both ions and electrons for non-radial IMF.

2.2 Initial conditions

In IAPIC, the spatial and temporal scales (mass ratio and charge to mass ratio, etc …) are chosen in order to be able to regenerate MHD large-scale classical structure of the Earth's magnetosphere (e.g., Omidi et al., 2004). For their modeling, Samsonov et al. (2017) used MHD and Community Coordinated Modeling Center (CCMC) resources, while the observational data are obtained from ACE, THEMIS and WIND spacecraft. Samsonov

²⁴⁷ et al. (2017) studied the impact of non-radial IMF , using a cone angle threshold value

²⁴⁸ of 50° on the magnetopause size and shape. Contextually, in the current study, we used

²⁴⁹ the physical parameters they used in their MHD initial conditions and scaled them to the

²⁵⁰ IAPIC initial condition values not only for non-radial IMF (where B_x and B_y are dominant

²⁵¹ over B_z, upper limit cone angle case of Samsonov et al. correspond to their threshold

²⁵² value), but also for purely radial IMF (where B_y and B_z are absent). The purely radial

²⁵³ IMF is an additional case included to study differences and similarities with the non-radial

²⁵⁴ nature of IMF on both magnetopause's shape and size and their role in creating dawn-dusk

²⁵⁵ asymmetries. The initial conditions of Samsonov et al. (2017) and our two IMF orientations

²⁵⁶ are then tabulated in Table 3.

Table 3. MHD initial conditions and their corresponding IAPIC scaled values for radial and non-radial IMF orientation(Samsonov et al., 2017).

Physical Units		Code Units	
Parameters	MHD	IAPIC$_\text{radial}$	IAPIC$_\text{non-radial}$
$N_{SW}(n/cc)$	2.606	4.	4.
T_{sw} (Kelvin)	32263	5×10^{-4}	5×10^{-4}
V_x (km/s)	-470.69	0.1412	0.1412
V_y (km/s)	-7.80	0	0
V_z (km/s)	-5.09	0	0
IMF$_x$ (nT)	-2.2	0.25	0.25
IMF$_y$ (nT)	2.99	0	-0.34
IMF$_z$(nT)	0.659	0	0.075
Tilt angle	31°	31°	31°
Initial Cone Angle(θ_{Bx})	54°	0°	54°
Initial Clock Angle(θ_{CA})	77.6°	Undefined	77.6°

3 Simulation Results

To our knowledge, a full 3D global kinetic modeling of radial IMF impacts on the dynamics of the magnetosphere has not been published, though the backstreaming of ions in the solar wind flow has been theoretically discussed (e.g., Willis, 1978, Eq. 3). The non-radial IMF event on July, 16th, 2007 observed by the THEMIS probes was chosen because it has been the subject of several detailed studies (Jelínek et al., 2010; Suvorova et al., 2010; Samsonov et al., 2017). The solar wind parameters and initial conditions were scaled for IAPIC as described in section 2. For purposes of comparison, we discuss in detail the plasma properties at the time step $3700\Delta t$ of our simulation for both purely radial and non-radial IMF (IMF orientation corresponding to the threshold cone angle value $\simeq 50°$ used by Samsonov et al. (2017) as described in the introduction). This time step corresponds to ≈ 24 minutes of real time, a relatively long enough period to perform a kinetic simulation of the dayside magnetosphere. In the following, IAPIC simulation results are analyzed to determine the magnetopause shape, size and location for the two IMF conditions considered, which give us a good frame to characterize any dawn-dusk asymmetry in the system.

3.1 Magnetopause response to radial and non-radial IMF

We derive the magnetopause's size from the location of the vertical cut of the maximum density gradient steepening using the number density derivative to get the maximum steepening (e.g., Garcia & Hughes, 2007; J. Lu et al., 2015).

We also use the pressure balance method to derive the MP location, a technique that offers an opportunity to explicitly include kinetic effects. Basically, in the pressure balance method, the dynamic and thermal pressures counterbalance the dipole magnetic pressure. Because of the magnetic field axis tilt $-31°$ at the time of THEMIS observation, the system is inherently asymmetric and the Cartesian grid used in the IAPIC simulations is not adequate to accurately derive a density gradient in most planes, particularly in the tilted magnetic equatorial plane. To overcome this difficulty, we transform our Cartesian 3D sim-

ulation box quantities (density, velocity vector, ...etc, at (x,y,z) positions) into a spherical 3D domain (same quantities at (r, θ, ϕ) positions), at the price of losing data from regions outside a spherical volume of radius equal to the smallest dimension of the initial Cartesian box (the Dusk-Dawn and South-North in our case). Our study does not suffer for that limitation because the dayside MP, our region of interest, is located inside the selected spherical domain. After checking that both reference frames provide the same spatial distribution of all physical quantities along the Sun-Earth (OX), the Dusk-Dawn (OY), and South-North (OZ) axis, we focus on deriving the magnetopause size at two key planes, namely the tilted magnetic equatorial plane $\theta = -31°$ and the plane $\theta = 0°$ that contains the Sun-Earth line. To quantify the MP expansion, we inject our initial solar wind conditions in physical units into the Shue model (Shue et al., 1997), which leads to a MP size equals to 10.3 R_E. Therefore, this MP size will be used as the reference in the current study. Our findings are summarized and tabulated in Table 4.

To better visualize asymmetries on large scales of the system, we introduce various contour plots that show a 2D cut of the plasma density distribution and magnetic field topology in 3 planes as shown in Fig. 2 and 3. The dipole field tilt of ($-31°$, North summer) seemingly has an impact on the macrostructure of the magnetospheric dynamics. Fig. 2a-c (d-f) show the 2D contour plots for plasma distribution along the Sun-Earth axis, the Dusk-Dawn axis, and South-North axis for radial IMF (for non-radial IMF).

Fig.2a&d clearly show the ($-31°$) tilt angle between the Sun-Earth axis (OX) and the magnetic equator axis for radial and non-radial IMF, respectively. Therefore, the forefront of the solar wind coplanar inflow approaches the planet and hits the upper boundary of the magnetosphere before it comes in head-on combat with the magnetic equator axis. This results in squeezing the magnetopause at high latitude and relaxes it in lower latitude. This torque-like effect generates plasma streaming that has a flare out configuration for radial IMF and a confined configuration for non-radial IMF as in Fig. 2d. For both IMF orientations, localized density maximas (yellow areas) can be seen at the subsolar point

310 (stagnation region) close to OX although being extended southward for the non-radial case.

311 These regions extend azimuthally duskward for both IMF orientations (Fig. 2b&e). Also,

312 large denser regions are present near the north cusp for both orientations although a smaller

313 one can be seen near the south cusp too for the non-radial case. In the linear plot Fig. 8, it is

314 seen like a hump at $\approx -16R_E$ along the Sun-Earth line for non-radial IMF. We do not know

315 why this layer appears for non-radial but not for radial IMF. The relaxation of the southern

316 part of the magnetosphere showed a denser plasma population up to $30R_E$ tailward and

317 flared in toward north at around $25R_E$ for non-radial IMF in Fig. 2d. The cavity around the

318 planet position is smaller and more confined in the non-radial IMF case than in the radial

319 IMF case. Moreover, Fig. 2b&e show the equatorial plane plasma distribution for radial and

320 non-radial IMF, respectively. Particle entry inside the magnetosphere is largely distributed

321 around the planet making the cavity reaches $\pm 5R_E$ along the Dusk-Dawn direction and

322 around $3R_E$ tailward, with plasma tube along the Sun-Earth line up the planet position.

323 On the other hand, the effect of B_y for the non-radial IMF in Fig. 2e, shows that the

324 magnetopause is compressed on both dusk and dawn sides. The cavity around the planet

325 is more confined and reduced in size to $\pm 5R_E$ along South-North direction for radial IMF,

326 and $\pm 4R_E$ for non-radial IMF, respectively (Fig. 2c&f). The plasma density in the South-

327 North/the Dusk-Dawn plane for radial IMF (Fig. 2c) shows denser plasma in the dusk sector

328 from -10 to -20 R_E than in the dawn sector from 10 to 20 R_E, while in the northern sector

329 there is a denser plasma that extends from around 10 to $17R_E$ but not regularly structured

330 with same thickness in the southern sector. It appears that there is a finger-like structure

331 (particle entry, small blue region) at around $-5R_E$ on the duskside that has an extension

332 of about $1R_E$ in the cavity around the planet. On the other hand, for non-radial IMF the

333 plasma distribution contour shows smaller cavity size and also a denser plasma on the dusk

334 side(Fig. 2f).

335 Fig. 3 shows the corresponding magnetic field lines topology of plasma density contour

336 shown in Fig. 2, respectively. This figure sheds light on the differences and similarities

337 between two IMF orientations along three different planes.

338   In Fig. 3a, the radial IMF field lines along OX are horizontal at $-20R_E$ and $\pm3R_E$ along

339   South-North direction and seen curled at $\pm10R_E$. At the magnetopause position, the field

340   lines divert at f(x,z)=$(-10,-8)R_E$. On the dayside magnetosphere, there are two potential

341   lobe magnetic reconnection sites(MR) sites. They are approximately located in the south-

342   ern hemisphere at f(x,z)=(0.5,-12) and at (-7.6,11.9)R_E in the northern hemisphere. The

343   magnetic field line topology shown in Fig. 3d is horizontal in the undisturbed SW; this

344   was not the case in Fig. 3a. This difference is attributed to the impact of B_y. In Fig. 3d

345   potential lobe MR sites are seen also at f(x,z)=(-8.,-12.) in the southern hemisphere and

346   at $(5,15)R_E$ in the northern hemisphere. Constant attention should be made when looking

347   at Fig. 3b, taken in the equatorial plane, because of the dipole tilt, what is shown here

348   for radial IMF is the high latitude magnetopause along OX in the Dusk-Dawn direction.

349   It is found that field lines from IMF connect to dipole field and permit particle entries at

350   that latitudes. The wavy structure in the night-side (not the focus of the current study)

351   indicates a complex current system induced at that distance. A potential MR site is shown

352   at f(x,y)=$(-7.6,9.9)R_E$. The curling of magnetic field lines at f(x,y)=(5,-15), (-15,-7)R_E

353   corresponds to the plasma dynamics shown in Fig. 2d. Same in Fig. 2e for non-radial IMF,

354   the curled magnetic field lines at a latitude corresponding to $\approx 6R_E$(north) are directed

355   toward dusk-midnight direction. Potential MR sites are at f(x,y)=(4.4,5.9), (-8.6,0.1), (3.5,-

356   7.9)R_E. In Fig. 3c, the magnetic field topology shows a more extended structure of closed

357   magnetic field lines for both duskside and dawnside than the non-radial case. The regions

358   extends until $\approx \pm14R_E$ along the dusk-dawn axis and reach up $\pm12R_E$ along the south-

359   north axis. In contrary, Fig. 3f shows different structures, where the extension of field lines

360   is less important along the dusk-dawn axis due to large scale connections of planetary and

361   interplanetary magnetic field lines and clear MR sites located in the southern hemisphere on

362   both dusk and dawn sides at f(y,z)=(-12.5,-2.6),(14.,-3.)R_E, respectively. Such reconnection

363   sites are not present (at least in this plane) for the radial case. The detailed investigation of

364   the MR regions is out of the scope of the present study yet these results suggest that these

365   reconnection regions are formed in the northern and southern lobe regions and extend to

366 the dawn and dusk flanks. They could lead to the squeezing of the dusk and dawn flanks of

367 the magnetopause seen in Fig. 2e.

368 In the first step, we focus on the direction defined by $\phi = -180°$ in both planes.

369 Using the maximum density steepening technique, we derive comparable values for the

370 magnetopause position at (~ 10.6, ~ 11.0) R_E, respectively for radial and non-radial IMF

371 along the Sun-Earth axis. We also obtain the same size when the effect of backstreaming

372 ions is removed (by post-processing) from the bulk flow for both IMF orientations. It would

373 suggest as it will be confirmed below that while the contribution of the backstreaming ion

374 population to the total density is small and does not change the location of the density

375 gradient maximum their contribution to the total pressure is important. In particular,

376 finite Larmor radius effects are more important for energetic ions. Along the tilted magnetic

377 equatorial axis, the magnetopause positions are (11.6, 12.0) R_E with bulk flow, which also

378 remain unchanged without backstreaming ions, respectively for the two IMF conditions.

379 First, we note that the different magnetopause positions derived from the IAPIC simu-

380 lation are all larger than the expected magnetopause position (~ 10.3 R_E) derived from the

381 Shue model (Shue et al., 1997). We remind that this reference MP size corresponds to the

382 initial solar wind physical parameters used in our simulations. All values derived show a

383 sunward expansion of the magnetopause position along the two selected axes. The magne-

384 topause appears to be subjected to a reduced SW dynamic pressure that allows the dipole

385 magnetic field network to expand outward. Based on the maximum density steepening tech-

386 nique, it is remarkable that our model predicts the magnetopause expansion self-consistently

387 in the range (0.3-1.3) R_E along the Sun-Earth axis and tilted magnetic equatorial axis for

388 the radial IMF case but also (0.7-1.7) for the non-radial IMF, respectively.

389 In the following, we explore our 3D IAPIC simulation results to try to uncover potential

390 processes that could be at the origin of the measured expansion. Since early reports, several

391 studies pointed to the potential impact of kinetic effects, particularly with the detection of

392 the signature of particles streaming in a direction opposite to the solar wind (Spreiter &

393   Alksne, 1969; Willis, 1978; Sibeck et al., 2001; Samsonov et al., 2017). As IAPIC simula-

394   tions offer the access to all populations of particles (macro-particles) with specific kinetic

395   properties, we tried to extract those particles on the dayside that move sunward, against the

396   main impinging solar flow. That statistical sub-population of particles has its own kinetic

397   properties and most importantly counterbalances the ram pressure of the incident solar flow,

398   as if it was originating from the magnetosphere and flowing outward. It is important to

399   stress that this population has kinetic properties (temperature, speed, etc.) much different

400   from the planetary ionospheric population that flows from the plasmasphere or the polar

401   wind, In Fig. 4, bulk pressures (dynamic, thermal denoted P_{dyn} and P_{thm}, respectively)

402   are shown with and without taking into account the contribution of backstreaming ions

403   to highlight the difference they make in the pressure balance. First, we remark that the

404   thermal pressure is dominant over dynamic pressure in the magnetosheath as expected for

405   a conversion of the convective flow energy to thermal energy after the bow-shock crossing.

406   P_{dyn} and P_{thm} cross P_{mag} at two points, i.e. with and without backstreaming ions included.

407   The corresponding size of the MP is $\sim 10.8 R_E$ for radial IMF and $\sim 11.7 R_E$ for non-radial

408   IMF along the Sun-Earth axis. Importantly, if the backstreaming ion effect is removed,

409   then the magnetopause size drops down to 10.5 and $11.4 R_E$ for the same IMF orientations,

410   respectively. The magnetopause is also measured along the tilted magnetic equatorial axis

411   with and without backstreaming ions and found equal to 11.9, $11.5 R_E$ for radial IMF and

412   12.0, $11.6 R_E$ for non-radial IMF, respectively. To summarize, these findings are tabulated

413   in Table 4. It is worth noting that the expansion ranges when using the pressure balance

414   method for deriving the MP size is slightly different from that using the density steepening

415   method. For example, the MP expansion rate is 0.5-$1.4 R_E$ for radial and non-radial IMF

416   along the Sun-Earth axis, compared to 0.3-$0.7 R_E$ derived by maximum density steepening

417   method. The difference between the two measurements is 0.2-$0.7 R_E$. The expansion range

418   is 1.6-$1.7 R_E$ as derived by pressure method compared to 1.3-$1.7 R_E$ as measured by density

419   steepening method, respectively along tilted magnetic equatorial axis. With only a differ-

420   ence between the two methods of $0.3 R_E$ for radial IMF and similar values for non-radial IMF

⁴²¹ along the tilted magnetic axis. Surprisingly, both methods suggest that the magnetopause

⁴²² expansion at the subsolar point is larger for the non-radial case than for the radial case. It

⁴²³ is probably the effect of the diffuse backstreaming ions in the case of non-radial IMF which

⁴²⁴ are hotter than that of radial IMF which explains the expansion toward the sun as well, as

⁴²⁵ a reference is the cross-field diffusion discussed in (Tsurutani & Lakhina, 1997; Paschmann

⁴²⁶ et al., 1981).We emphasize that the ring current that generates the dipole field for both

⁴²⁷ radial and non-Radial IMF is the same. That's to say, the solar wind conditions, and the

⁴²⁸ dipole strength are the same for both IMF cases, except for the non-radial IMF, where B_y

⁴²⁹ is dominant over B_x and B_z. Therefore, any noticeable differences such as the larger MP

⁴³⁰ expansion is directly related to the presence of the IMF B_y. It is worth to continue broadly

⁴³¹ investigating the radial IMF by PIC code to better understand the related physics that

⁴³² handle this problem.

Maximum Density Steepening magnetopause derivation

IMF /Axis	The Sun-Earth Axis		Tilted Magnetic equator axis	
Kinetic effect	Yes	No	Yes	No
magnetopause for radial IMF	10.6 R_E	10.6 R_E	11.6R_E	11.6R_E
magnetopause for non-radial	11.0R_E	11.0 R_E	12.0R_E	12.0R_E

Pressure balance magnetopause derivation

IMF/Axis	The Sun-Earth Axis		Tilted Magnetic equator axis	
Kinetic effects	Yes	No	Yes	No
magnetopause for radial IMF	10.8R_E	10.5 R_E	11.9 R_E	11.5R_E
magnetopause for non-radial	11.7 R_E	11.3 R_E	12. R_E	11.6 R_E

Table 4. Summary of results for the MP location is tabulated as derived by density steepening method (derivative of number density) and pressure balance methods for both IMF orientations. The values are measured on both the Sun-Earth Axis and tilted magnetic equatorial axis. The kinetic effect is when the bulk flow (including backstreaming ions) is considered, and its absence when inflow (earthward) only is considered. The reference size for these values is $10.3R_E$.

433   In their papers, Bonifazi and Moreno (1981b, 1981a) used ISEE2 data of 3253 ion

434   spectra that correspond to ≈ 90 hours, studying the density and energy of the backstreaming

435   ions. They quantitatively characterized them into three categories. The authors used a

436   scaling factor such that the ratio (A) of the backstreaming bulk speed over their thermal

437   speed to identify the following three populations: ≥ 1.2 for reflected ions, ≤ 0.8 for diffuse

438   ions and an intermediate population $0.8 \leq A \leq 1.2$.

439   Here, we adopted their method to quantify the characteristics of the backstreaming ions

440   in the dayside solar wind flow. First, a simple statistical study of the dayside populations

441   shows that the solar wind bulk flow is composed by 16.5% and 20% of backstreaming ions

442   for radial and non-radial IMF, which confirms that their contribution to the total density is

443   small whereas its contribution to the total pressure can be crucial. Fig. 5a shows that, for

444   radial IMF 72.5% of backstreaming ions are characterized as reflected ions and only 27.5%

445   as intermediate ($0.8 < A < 1.2$). For the non-radial IMF case, we found a totally different

446   characteristics for backstreaming ions. There are only identified as 21.6% reflected particles,

447   31.4% intermediate particles and 47.0% diffuse particles along the same OX axis. To follow

448   up the impact of the tilted magnetic axis on the particles populations, we also conducted

449   the same statistical analysis on the tilted magnetic equatorial axis. We found for radial

450   IMF that 59% of ions are reflected and 41% are in the intermediate phase. On the other

451   hand, backstreaming ions are characterized as 23.5% of reflected ions, 53% of intermediate

452   case, and finally 23.5% for diffuse ions for non-radial IMF. In Fig. 5 we found that for radial

453   IMF, on both axis, most of the backstreaming ions are in the reflection mode, with a small

454   percentage in intermediate mode at the bow shock. On the other hand, for non-radial IMF,

455   on both axis, backstreaming ions are in intermediate and diffuse mode in the solar wind,

456   but the reflection mode appears to be dominant around the bow shock.

457   Still, to better understand the kinetics of the distribution of the backstreaming ions,

458   we show in Fig. 6 the velocity distribution function (VDF) of solar wind ions along the

459   Sun-Earth line as far as $-20R_E$. For the purely radial IMF case, a substantial fraction

460 of VDF spatial distribution of backstreaming ions is found in the three planes (XZ, XY

461 and YZ) whereas only a small fraction is obtained for non-radial IMF, especially in the YZ

462 plane. The VDF in Fig. 6a shows the reflection of the plasma sunward and southward for

463 radial IMF, with minor reflection for non-radial IMF but larger distribution toward north

464 and earth direction as confirmed by Fig. 5. It is also found that at Y=Z=0 and X=-20R_E

465 that the reflection of backstreaming ions are larger for radial than non-radial IMF. While

466 on the other hand in Fig. 6c&f, the spatial distribution of ions is reflected mostly toward

467 the south and sunward for radial and mostly toward north for non-radial IMF.

468 In the following, we track the magnetopause shape for both IMF orientations in two

469 different locations. In order to handle the complex geometry of the tilted dipole, we use

470 spherical coordinates such that ϕ=-180° at the dayside standoff distance (θ =0) along the

471 Sun-Earth Axis and (θ=-31) along the tilted magnetic equatorial axis. In that frame, we

472 track the shape every 20° along ϕ in two different axes. The MP shape for the two IMF

473 orientations is constructed in the XY-plane and in the magnetic equator that both contain

474 the dusk-dawn direction. In Fig. 7, the MP is shown in the half-plane that contains dawn

475 (positive Y), so that the asymmetry between dusk and dawn clearly appears using a mirror

476 image of the MP shape in the dusk half-plane that is over-plotted on the dawn half-plane.

477 For example for the radial case, Fig. 7a&b show a small the dusk-dawn asymmetry for the

478 two selected planes (i.e. XY and tilted magnetic equator planes) whereas this asymmetry

479 is more important in the non-radial case; the duskside magnetopause being more extended

480 than the dawnside (Fig. 7c&d).

481 In particular Fig. 7c, the MP along the Sun-Earth axis is squeezed earthward on the

482 dawnside down to 7.5R_E whereas the dusk sector spreads out to $\approx 12R_E$. In Fig. 7d, we

483 have a peculiar non-symmetric MP shape in the magnetic equator with a size $\approx 10R_E$

484 except near the Y-axis. In Fig. 8, the linear densities for both IMF orientations are plotted

485 in three different directions. For purely radial IMF (Fig. 8a&b, ion and electron densities

486 are over-plotted along the Sun-Earth line (upper panel OX,Y=Z=0) from -20 to -10R_E,

the Dusk-Dawn line (middle panel OY, X=-13, Z=0) from -20 to +20, and South-North line (lower panel OZ, X=-13, Y=0) measured. Densities in OY, and OZ panels are aimed to show the density profile just outside the MP position taken at -13R_E. The vertical dashed line in the upper panel shows where the densities are plotted in the other two directions. Fig. 8 shows the quasi-neutrality of the solar wind, magnetosheath and magnetospheric plasmas. Ion and electron densities are correlated with no charge separation. Also, it is found that along the Dusk-Dawn axis and South-North axis taken just outside the MP there is an apparent asymmetry at both the dusk-dawn and south-north directions. For both IMF orientations, magnetosheath densities are larger on the duskside than on the dawnside and larger in the southern hemisphere than in the Northern.

For the non-radial case (Fig. 8b), we notice a hump/heap just upstream of the bow shock position at $\approx -16R_E$. We tracked backstreaming ions at that distance and only a little fraction was found. Its type corresponds to reflected ions according to the characterization of backstreaming ions reported in Fig. 5. The plasma jump at X = -16R_E reaches factor 2. The same value is found when we perform a cut along OY and OZ at X=-16 R_E (not shown) indicating that this jump is at a large scale and present across the full magnetosheath. The other major components of the solar wind dynamics is related to the ion velocity modulus that is shown in Fig. 9 in the same order. The density hump in Fig. 8b corresponds to a velocity decrease in Fig. 9b.

The temperatures of solar wind particle species are important to identify boundary crossing, for instance, between the cold component of the solar wind and the hotter component of the magnetosheath plasma. Furthermore, ion-to-electron temperature T_i/T_e is approximately conserved at the MP boundary (Wing et al., 2014). The T_i/T_e ratio in the magnetosheath was thoroughly investigated by Lavraud et al. (2009). In the current paper, the (T_i/T_e) ratio of the impinging solar wind is depicted in Fig. 10. For radial IMF Fig. 10a, T_i is slightly fluctuating in the solar wind until it increases by a factor 2 between -15 to -12 R_E along OX as expected due to the shock crossing which slows down and heats the

514   plasma; then it decreases downstream before it increases again in the magnetosheath until

515   it reaches the MP position. While on the other hand, the electron temperature T_e in the

516   magnetosheath maintains a constant value and has increased by a factor 1.2 compared with

517   the electron temperature in the solar wind. The average (T_i/T_e) ratio in the magnetosheath

518   is ≈ 1.72. The temperature profile for the non-radial IMF case shown in Fig. 10b is dif-

519   ferent from the purely radial IMF case. T_i starts constantly increasing at $-15R_e$ including

520   the bow shock and the magnetosheath. From the solar wind to the magnetosheath, T_i in-

521   creases by a factor 4. On the other hand, T_e starts increasing at $-16R_E$ and keeps rising

522   through the magnetosheath. The average (T_i/T_e) ratio in the magnetosheath is ≈ 1.1. The

523   ion-to-electron temperature ratio is discussed more in detail in section 4

524   The temperature anisotropy was studied extensively in the past (Gingell et al., 2015;

525   Karimabadi et al., 2014; Treumann & Baumjohann, 2013). In the current paper, we were

526   able to derive the temperature anisotropy of the solar wind particle species. Fig.10c shows

527   for radial IMF, the average ion temperature anisotropy $T_{\perp i}/T_{\parallel i}$. In the dayside sector

528   (between -18 and -10 R_E) this ratio is ≈ 2. and inside the magnetosheath (between -14 and

529   -12.5 R_E) it reaches 2.7. Therefore the perpendicular ion temperature anisotropy is stronger

530   in the magnetosheath than in the solar wind. The maximum ratio is found at the bow shock

531    $(\sim -14R_E)$ with a factor of 3.3. The average electron temperature anisotropy $T_{\perp e}/T_{\parallel e}$ in

532   the dayside sector equals to ≈ 2.3, which is almost the same as inside the magnetosheath.

533   Fig. 10d displays for the non-radial IMF orientation, the anisotropy average for ions in the

534   dayside sector (between -18 and -10 R_E along OX). The $T_{\perp i}/T_{\parallel i}$ ratio ≈ 6 for ions and

535   ≈ 1.8 for electrons. In the magnetosheath (between -14 and -12.5 R_E along OX) $T_{\perp i}/T_{\parallel i}$

536   ratio is 3.2 whereas electron temperature is quite isotropic. These results will be discussed

537   in section 4.

538   **3.2 Dawn-Dusk asymmetry in the dayside magnetosphere under the influ-**

539   **ence of radial and non-radial IMF**

540   The large scale results reported above all indicate systematic asymmetries in the Dusk-

541 Dawn and South-North directions for the two IMF orientations. In the following, we try

542 to quantify those asymmetries, particularly in the Dusk-Dawn direction for the radial and

543 non-radial IMF cases we have simulated. Figures 2b,c,e,f,7, and 8 visually show asymmetry

544 in the Dusk-Dawn direction.

545   Fig. 2b,e show the Dusk-Dawn asymmetry along the Sun-Earth direction (OX) and

546 Fig. 2c,f show the asymmetry along the Dusk-Dawn (OY) and South-North (OZ) directions.

547 The linear density plots are shown in Fig. 8, middle panel, plotted along the dusk-dawn

548 direction at $X \approx -13 R_E$. The asymmetry in the South-North planes can be seen in Fig. 8

549 lower panel. In Fig. 11, some solar wind parameters i.e. N_i, V_i, and T_i, and Fig. 12 B_x,

550 B_y and B_z are plotted along three different axes (parallel to OX) for each IMF orientation.

551 Two of which are plotted at $Y = \pm 6 R_E$ on both sides of OX axis, and the third along the

552 Sun-Earth line from -18 to 10.8 and 11.7 R_E for radial and non-radial IMF. Dashed lines

553 are the calculated positions of the MP at dawn and dusk ($Y = \pm 6 R_E$, green and red dashed

554 lines, respectively) and along OX ($Y = 0$, blue dashed line) as measured from the gradient

555 density method (same as shown in Fig. 7).

556   In the magnetosheath, left to the vertical blue dashed line, all plasma parameters

557 are asymmetric. On the dusk side (red dashed line), the MP position is located at -8.5,

558 and -7.7R_E for radial and non-radial IMF. Whilst on the dawn side (green dashed line),

559 it is located at -7, and -5.2 R_E. For both IMF orientations, ion density increase in the

560 magnetosheath is larger on the duskside than on the dawnside (Fig.11). The largest increase

561 is along the symmetry axis (OX). For the radial case, ion velocity (V_i) decreases after the bow

562 shock crossing along (OX) whereas this deceleration is less important for both dawn and dusk

563 sides until reaching the magnetopause. For the non-radial case, the same behavior is shown

564 along (OX) whereas the ion flow seems to accelerate until the magnetopause crossing on the

565   duskside and to decelerate on the dawnside even more than along (OX). Ion temperature

566   T_i in the solar wind and in the magnetosheath is larger on the dawnside for the radial case

567   whereas it does not show any the dusk-dawn asymmetry for the non-radial case. In Fig. 12,

568   for both IMF orientations, B_z becomes positive close to the magnetopause likely due to

569   the draping effect. Furthermore, the large initial IMF B_y of non-radial case (positive in

570   GSE, negative in IAPIC coordinates=-0.34) remains quite constant and homogeneous in

571   the solar wind and magnetosheath regions. For the radial case, the By component is more

572   variable and different between dusk and dawn side in the solar wind and magnetosheath

573   regions. Initial IMF B_x (negative in GSE and positive in IAPIC coordinates =0.25) does

574   not remain constant and shows the Dusk-Dawn asymmetry. A large increase occurs only

575   in the dawn magnetosheath sector. For the non-radial case, Bx remains quite steady in the

576   dayside region but is larger on the duskside than along OX and on the dawnside where the

577   initial value has been reduced.

4 Discussion and Analysis

579   As described in section 3.1, we derived the MP position (10.6,11.0) R_E along the Sun-

580   Earth line for purely and non-radial IMF, respectively (using the location of the maximum

581   number density gradient). In addition, we have shown that PIC simulations offer the pos-

582   sibility to isolate backstreaming ions from the pool of particles in the box simulation. This

583   process allows us to derive their contribution to the dynamic and thermal pressures in the

584   dayside magnetosphere. It is important to stress that other complex effects could be in-

585   duced by the presence of those backstreaming particles, like induced currents and fields, that

586   will be considered in a future study. Subtracting the contribution of backstreaming ions in

587   the ensemble average of the plasma properties increases the resulting system pressure and

588   consequently moves the magnetopause location toward Earth.

589   Using the balance between ram pressure and magnetic pressure (e.g., Willis, 1978, Eq.

590   3) we were able to derive the MP size in different planes with and without backstreaming

ions (Table 4). These calculations reveal the impact of backstreaming ions in reducing the solar wind dynamic pressure allowing for MP expansion by 0.3-0.4R_E. All our findings above also suggest the important results that by neglecting ions kinetic effects, MHD simulations implicitly overestimate SW pressure in the dayside region and underestimate the MP size.

For instance, the MP expansion range derived here is consistent with the expansion observed by THEMIS spacecraft for the event of 16 July 2007. To get the observed expansion with their MHD model, Samsonov et al. (2017) were forced to modify the solar wind properties, propagated from WIND and ACE *in situ* measurements, of their boundary conditions. This means that a non-negligible fraction (up to $\sim 40\%$) of the observed expansion that is due to backstreaming particles was modeled in their study by an ad hoc reduction of the SW dynamic pressure.

We conclude that the dynamic pressure of backstreaming ions contributes significantly to the expansion/compression of the magnetopause. Note that when the magnetopause is derived from the density maximum steepening, the effect of the backstreaming ions is not significant as their contribution to the total density is small. This indicates that the main driver of the expansion of the magnetopause is the upstream reduction of the solar wind dynamic pressure in the dayside region due to the reduction of the solar wind bulk flow by the presence of the backstreaming ions, which although being a small percentage of the total solar wind ion population (16.5% and 20% for radial and non-radial IMF, respectively) have a strong effect on the dynamic pressure. More generally, the insensitivity of the MP size to the density of backstreaming ions confirms the conclusions reported in (Samsonov et al., 2020, Eq. 2), that density and velocity (dynamic pressure) might have different contributions to the effective values of the dynamic pressure component in the pressure system balance used in driving the magnetopause position. This appears clearly in our results in Table 4.

However one can notice that for the non-radial case with a large positive IMF B_y component, the effect of backstreaming ions could have been expected to be more important on the dawnside where the foreshock region is moved leading to a pronounced magnetopause

expansion on the same side. Instead, we found that the magnetopause is moved earthward in both dawn and dusk sectors. We suspect that this effect could be due to the formation of magnetic reconnection regions across the dayside magnetopause seen in Fig. 3 in these specific IMF conditions (with a clock angle of 77.6°, a cone angle of 54° and a large dipole tilt of −31° corresponding to a North summer time) rarely investigated in past studies (e.g., Trattner et al., 2007). Indeed, the dayside reconnection process is known to erode the magnetopause therefore moving earthward the magnetopause boundary. Our results could suggest that the reconnection process which erodes the magnetosphere could dominate against the effect of the backstreaming ions which tend to expand the magnetopause. The detailed investigation of the magnetic reconnection process in our simulations is out of the scope of the present study and will be addressed in a further study.

Using THEMIS measurements, Wang et al. (2012) showed how the T_i/T_e ratio changes in the magnetosheath and the plasma sheet. They showed that $T_i/T_e \approx 4 - 12$ in the magnetosheath. In the tail plasma shee, this ratio spans $\approx 6 - 10$. Other studies statistically examined the T_i/T_e in different regions in the magnetosphere to find a ratio $\approx$ 6-12 close to the magnetopause (Lavraud et al., 2009, and references therein) . On the other hand the T_i/T_e ratio was as low as ≈ 3 at the magnetosheath flanks (Lavraud et al., 2009). In the current paper, we show in Fig. 10a&b, the ion and electron temperature ratio T_i/T_e in the dayside region. In the magnetosheath this ratio is found about 1.72 and 1.1 for radial and non-radial IMF, respectively (Dimmock et al., 2014, 2015).

On the other hand, the presence of backstreaming particles should also affect the temperature anisotropy in the dayside region ahead of the magnetosphere. Grygorov et al. (2017); Samsonov et al. (2012) showed that the temperature anisotropy in the magnetosheath controls the pressure distribution near the magnetopause. Here we found that the ion temperature anisotropy ratio is about 2 in the magnetosheath for radial IMF, and about 6 for non-radial IMF (Fig.10c&d), consistent with Wang et al. (2012). Analysis of

the temperature distributions will be used in future work to study microinstabilities and reconnection.

To characterize the kinetic properties of the backstreaming particles, we have first used the nomenclature of Bonifazi and Moreno (1981b) and obtained results given in section 3. In Table 5, we show the bulk speed of backstreaming ions in real physical units in accordance with the characterization factor reported in (Bonifazi & Moreno, 1981b). It is found that for both IMF orientations and along both axes, the magnitude of the bulk velocity of the backstreaming ions (directed sunward) is larger than the full solar wind velocity. Despite a relatively small percentage of the total ion population, backstreaming ions reduce significantly the solar wind velocity. Furthermore, thermal velocities of backstreaming ions are larger for the non-radial case than for the radial case, suggesting that heating of backstreaming ion is more important in the non-radial case.

The second major finding of this study is the Dawn-Dusk asymmetry. Uncovering its origin is important for better understanding, modeling and prediction of space weather phenomena (e. g., S. Lu et al., 2016). Asymmetry is observed by Cluster spacecraft in north-south magnetotail planes (Haaland et al., 2017; Samsonov, 2006) and in dawn-dusk planes (A. P. Walsh et al., 2014; Samsonov, 2011; Dimmock et al., 2017; Turc et al., 2020). Both observations and numerical simulations have revealed that the magnetopause size is a function of IMF strength and orientation, and solar wind dynamic pressure, which by turn modify the magnetopause shape and generate dawn-dusk asymmetries (Liu et al., 2019). Using data from IMP 8 and ISEE1, ISEE 3 and WIND, (e.g., Paularena et al., 2001, Table 3) showed a significant dawn-dusk asymmetry in the Earth's magnetosheath which is larger on the dawn side than on the dusk side, for all IMF orientation. They also showed that the IMF orientation impacts density asymmetry in dawn-dusk direction. Paularena et al. (2001) reported the same kind of asymmetry in different regions in the dayside magnetosphere in the Sun-Earth and the Dusk-Dawn plane. In their recent study, Turc et al. (2020) discussed the magnetosheath asymmetry in terms of IMF, solar wind

Total number of particles inside the simulation box

	Radial	non-radial
# bulk flow ions	5.38958×10^7	5.21372×10^7
# backstreaming ions	8.87744×10^6	1.07256×10^7
percentage	16.5%	20%

Backstreaming Ions Characteristics

	Radial		non-radial	
	OX	Tilt	OX	Tilt
reflected ions	72. %	58.%	22.%	24.%
intermediate ions	27. %	41. %	31.%	53.%
diffuse ions	1.%	1. %	47.%	23.%
$V_{bp}(km.s^{-1})$	373	392	294	346
$V_{thm}(km.s^{-1})$	254	255	321	332
$V_{sw}(km.s^{-1})$	287	254	233	248

Table 5. The ratio of backstreaming ions to bulk flow of the number density for both IMF orientations is shown in the upper panel. The backstreaming ions are characterized with three categories (see Fig. 5). Based on scaling factor ((Bonifazi et al., 1980)) the backstreaming ions are reflected, intermediate or diffuse. V_{bp} is the bulk flow of the backstreaming ions, V_{thm}, their thermal speed and their full solar wind velocity V_{sw} (including contribution of backstreaming ions) are shown in the lower panel for both IMF orientations along OX and Tilt axis. This data is measured at the dayside magnetosphere

density, velocity by using Vlasiator hybrid code (Palmroth et al., 2018). They found that magnetic field asymmetry and density variability in the magnetosheath are stronger when IMF tends toward a radial direction.Similarly, using IAPIC, the dawn-dusk asymmetry in the magnetosheath and in the solar wind is investigated. In our work, the MP shape in Fig. 7, shows how asymmetric the dawn-dusk sides are. A result that is confirmed in Fig. 11, and 12, IMF, density, temperature and ion velocity are tested at the the dusk-dawn flanks asymmetry in the magnetosheath. In the magnetosheath (left to the vertical blue dashed line) all plasma parameters are asymmetric which is consistent with recent results obtained by Turc et al. (2020). Furthermore, for both IMF orientations, the magnetopause is more extended on the duskside (red dashed line) than on the dawnside (green dashed line).

Finally, our analysis of the location, shape and size of the MP with the techniques developed for that purpose, in addition to the ability to quantify plasma parameters in 3D to track asymmetries in the dusk-dawn and south-north direction, our code is applicable to planetary and exoplanetary magnetospheres. Furthermore, our findings can also contribute to alternative methods for a better analysis of soft x-ray imaging of the magnetosphere (Sibeck et al., 2018) in a complementary manner. This includes the MP, the cusp dynamics, the magnetosheath that is related to density structure which can be deduced from soft x-ray observation.

Most current support to the SMILE mission is based on MHD modeling (SMILE working group). In light of the results obtained so far (see Figs. 4 and 7 , and Tables 4), our global 3D electromagnetic kinetic code provides another point of view on the range of expected boundary locations under various solar wind flux. An accurate estimation of those boundary locations are key to interpret the X-ray signal that will be detected by SXI, the SMILE X-ray detector. In addition, our simulations provide details about ions kinetic properties locally and on global scales (eg. Fig. 8), an additional tool for coupling plasma properties that will be detected by the light Ion Analyser (LIA) and large scale structure that will imaged by SXI. In light of the results obtained so far, we propose IAPIC, as a global 3D

698 electromagnetic kinetic code to simulate the MP, the cusps, and the magnetosheath, which

699 should enhance the science return of space missions like the CSA − ESA SMILE mission.

5 Summary and Conclusion

701 We have utilized a three-dimensional kinetic particle-in-cell code (IAPIC) to determine

702 the size, shape and location of the Earth's magnetopause with a dipole tilt of $-31°$ (North

703 hemisphere summer) in response to solar wind conditions of radial (B=Bx) and non-radial

704 ($|Bz| < |Bx| < |By|$) IMF. These two IMF orientations cover the range of non-radial IMF

705 with a cone angle between 0 and $50°$ as considered by Samsonov et al. (2017) related to

706 a magnetopause crossing event recorded by the THEMIS mission on 16 July 2007. The

707 simulations show sunward MP expansions and predict asymmetric magnetosphere for both

708 IMF orientations.

709 Using a reference MP size (10.3 R_E) independently derived from (Shue et al., 1997)

710 and based on our pressure balance calculations (Table 4), the findings of this study are

711 summarized as follows:

712 1. For purely radial IMF, the MP expands from 10.3 to $10.8R_E$ for the full bulk flow.

713 The expansion is limited to only $10.5R_E$ when the effect of the backstreaming ions

714 are dropped from calculations along OX axis. In other words, 40% of the observed ex-

715 pansion is due to backstreaming solar wind particles. Moreover, along tilted magnetic

716 axis, the MP expansion is from 10.3 to 11.9 and 11.5 with and without backstreaming

717 ion effect, respectively.

718 2. For non-radial IMF, the expansion is from 10.3 to 11.7 (along Ox) and to $12R_E$ (along

719 tilted axis) for the full bulk flow. It is limited to only 11.3 (along Ox) and $11.6R_E$

720 (along tilted axis) when backstreaming ions are not accounted for in the flow.

721 3. For non-radial IMF and full bulk flow (i.e., including the effect of backstreaming

722 ions), the expansion rate is 1.4 and $1.7R_E$ along OX and tilted magnetic equatorial

723 axis, respectively. These rates are comparable with the average expansion rate of

724      $1.3\text{-}1.5R_E$ reported from THEMIS observations (Jelínek et al., 2010; Suvorova et al.,

725   2010), without being forced to modify the input solar wind parameters as done by

726   MHD model (Samsonov et al., 2017).

727 4. The backstreaming ions contribution to the bulk flow is 16.5%, and 20% for radial

728   and non-radial IMF, respectively along the OX axis in the dayside magnetosphere.

729 5. When deriving the MP position using the maximum density steepening method, the

730   backstreaming ions (characterized and quantified in this study) do not impact the

731   measured size of the MP for both IMF orientations along both OX and tilted axis

732   since they represent only a small percentage of the solar wind plasma.

733 6. In contrast, when the magnetopause is derived using pressure system balance without

734   accounting the effect of backstreaming ions, the magnetopause expansion is reduced

735   by $0.3 - 0.4 \; R_E$ (Table 4).

736 7. The difference between magnetopause derivation using maximum density steepening

737   (Garcia & Hughes, 2007; J. Lu et al., 2015) and the pressure systems balance using

738   definition of dynamic pressure as in (e.g., Willis, 1978, Eq. 3) is consistent with the

739   conclusion drawn by (Samsonov et al., 2020) that density and velocity act differently

740   as a component of dynamic pressure in the pressure system balance. While the

741   energetic backstreaming ions have a small impact on the total density, they have a

742   significant contribution to the total dynamic pressure. In our study, we also considered

743   the effect of thermal pressure in the magnetosheath in the pressure balance.

744 8. At the subsolar point, the magnetopause expansion is larger for the non-radial case

745   than for the radial case (for both OX and tilted axes). However, in the non-radial case

746   both dawn and dusk magnetopause flanks are squeezed toward the Earth which could

747   be due to the reconnection process in these specific conditions (large IMF B_y, with a

748   clock angle of 77.6°, a cone angle of 54° and a large dipole tilt of 31° corresponding to

749   a North summer time) rarely investigated in past studies. The detailed investigation

750   of the magnetic reconnection process in such conditions is out of the scope of the

751   present work and will be carried out in a further study.

9. We present new results showing the magnetopause shape in spherical polar coordinates for the two IMF directions. This new technique along with the magnetopause derivations given in Table 4 and Fig. 4 enables us to anticipate the sizes, shapes and locations of magnetopause for all magnetized planets, including magnetized exoplanets. Additionally, this technique accounts for the backstreaming ion contribution to the data used to derive the magnetopause shape, a key information that is not available with other types of simulations.

10. The current study enabled us to derive the solar wind temperature anisotropy, thus paving a research road to study kinetic microinstabilities in the solar wind-magnetosphere coupling (see Figs. 10). In the dayside sector (between -18 and -10 R_E along OX) for non-radial IMF, $T_\perp/T_\parallel$ is large and equal ≈ 6 for ions and ≈ 1.8 for electrons. For radial IMF, $T_\perp/T_\parallel$ equals to 2. and 2.3 for ions and electrons, respectively. The $T_{\perp e}/T_{\parallel e}$ ratio can be employed to predicts whistler waves generated by temperature anisotropy like those observed by MMS (e.g., Le Contel et al., 2016). Temperature anisotropy is known to have important effects on the magnetic reconnection process (e.g., Gingell et al., 2015).

11. For both IMF orientations, the magnetopause is found asymmetric: its expansion is larger on the duskside than on the dawnside.

12. In light of the results so far obtained, our findings are considered an additional and key modeling supports to future near-Earth exploration projects, in addition to outer planets' moons and magnetospheres. For example, the newly developed technique to map the MP shape and position, or the ability to track backstreaming ions and their characterizations and their kinetic impact on the plasma flow will contribute to deepen our understanding about the kinetic behavior of plasma in the solar wind magnetosphere coupling and the study of exoplanets magnetospheres.

Future Directions

Radial and non-radial conditions are relatively infrequent configurations of the IMF at

Earth, but closer to the Sun, the Parker spiral would favor more and more non-radial IMF orientation (Chang et al., 2019). This suggests that radial IMF conditions are more common at Mercury, which has recently been investigated by MESSENGER and will soon be visited by the BepiColombo spacecraft. Furthermore, Mercury's magnetosphere is much smaller as the magnetopause standoff position is only at about $2R_M$ (R_M being the Mercury radius) and the ion gyroradius is about the size of the planet. Finite Larmor radius effects are expected to play an ever more important role than in the Earth's case (e.g., Johnson et al., 2014; Paral & Rankin, 2013). Mercury is therefore a natural laboratory for investigating radial IMF and related kinetic effects and we will prepare simulations in advance of Bepi-Colombo's arrival at Mercury. Planets even closer to their stars are common in the galaxy (NASA Exoplanets Archive $doi = 10.26133/NEA2$), suggesting that, particularly around cooler M- and K-type stars, radial IMF may be a common condition. This impacts the structure of their magnetospheres and may influence the escape of planetary atmospheric and ionospheric constituents over time. The kinetic aspect of our approach is particularly sensitive to the dynamics of the bow shock, which may be highly variable in the neighborhood of a small star (Cohen et al., 2015), potentially producing accelerated particles and observable radio emissions (Cohen et al., 2018). One more issue that will be considered for near future work is the impact of the magnetosphere-ionosphere-magnetosheath coupling on magnetopause location. We have tracked in the past $H^+$and O^+ ions outflow from the ionospheric origin in the dayside magnetosphere (S. M. Baraka & Ben-Jaffel, 2015). IAPIC can also be used to study the outflow of plasmasphere low energy ions.

References

Akasofu, S.-I. (1991). Development of magnetospheric physics. *Magnetospheric Substorms*, *64*, 3–9.

Akasofu, S.-I., Roederer, M., & Krimigis, S. (1982). Dawn-dusk asymmetry of the tail region of the magnetosphere of saturn and the interplanetary magnetic field. *Planetary and Space Science*, *30*(10), 1061–1063.

Artemyev, A., & Zelenyi, L. (2012, December). Kinetic Structure of Current Sheets in the Earth Magnetotail. *Space Science Reviews*, *178*(2-4), 419–440. doi: 10.1007/s11214-012-9954-5

Asbridge, J., Bame, S., & Strong, I. (1968). Outward flow of protons from the earth's bow shock. *Journal of Geophysical Research*, *73*(17), 5777–5782.

Baraka, S. (2016, April). Large Scale Earth's Bow Shock with Northern IMF as Simulated by PIC Code in Parallel with MHD Model. *Journal of Astrophysics and Astronomy*, *37*(2), 1–16. doi: 10.1007/s12036-016-9389-6

Baraka, S., & Ben-Jaffel, L. (2007, June). Sensitivity of the Earth's magnetosphere to solar wind activity: Three-dimensional macroparticle model. *Journal of Geophysical Research (Space Physics)*, *112*, 6212. doi: 10.1029/2006JA011946

Baraka, S., & Ben-Jaffel, L. (2011). Impact of solar wind depression on the dayside magnetosphere under northward interplanetary magnetic field. *Annales Geophysicae*, *29*(1), 31–46. Retrieved from https://www.ann-geophys.net/29/31/2011/ doi: 10.5194/angeo-29-31-2011

Baraka, S. M., & Ben-Jaffel, L. (2015). Magnetospheric dynamical and morphological response to multi-species plasma supply from the ionosphere: New comprehensive 3d pic simulation. *AGUFM*, *2015*, SM23B–2552.

Ben-Jaffel, L., & Ballester, G. (2013, May). Hubble Space Telescope detection of oxygen in the atmosphere of exoplanet HD 189733b. *Astronomy & Astrophysics*, *553*, A52. doi: 10.1051/0004-6361/201221014

Ben-Jaffel, L., & Ballester, G. E. (2014, April). Transit of Exomoon Plasma Tori: New Diagnosis. *apjl*, *785*, L30. doi: 10.1088/2041-8205/785/2/L30

Berchem, J., Richard, R. L., Escoubet, C. P., Wing, S., & Pitout, F. (2016, January). Asymmetrical response of dayside ion precipitation to a large rotation of the imf. *Journal of Geophysical Research (Space Physics)*, *121*, 263–273. Retrieved from https://ui.adsabs.harvard.edu/abs/2016JGRA..121..263B doi: 10.1002/2015JA021969

Blanco-Cano, X., Omidi, N., & Russell, C. (2006). Macrostructure of collisionless bow shocks: 2. ULF waves in the foreshock and magnetosheath. *Journal of Geophysical Research: Space Physics (1978–2012)*, *111*(A10).

Blanco-Cano, X., Omidi, N., & Russell, C. (2009). Global hybrid simulations: Foreshock waves and cavitons under radial interplanetary magnetic field geometry. *Journal of Geophysical Research: Space Physics*, *114*(A1).

Bobra, M., Petrinec, S., Fuselier, S., Claflin, E., & Spence, H. E. (2004). On the solar wind control of cusp aurora during northward imf. *Geophysical research letters*, *31*(4).

Bonifazi, C., & Moreno, G. (1981a). Reflected and diffuse ions backstreaming from the earth's bow shock 1. basic properties. *Journal of Geophysical Research: Space Physics*, *86*, 4397-4404. doi: 10.1029/ja086ia06p04397

Bonifazi, C., & Moreno, G. (1981b). Reflected and diffuse ions backstreaming from the Earth's bow shock 2. Origin. *Journal of Geophysical Research: Space Physics (1978–2012)*, *86*(A6), 4405–4413.

Bonifazi, C., Moreno, G., Lazarus, A. J., & Sullivan, J. D. (1980, November). Deceleration of the solar wind in the earth's foreshock region - ISEE 2 and IMP 8 observations. *textbackslashjgr*, *85*, 6031–6038. doi: 10.1029/JA085iA11p06031

Brackbill, J. U. (2011). A comparison of fluid and kinetic models of steady magnetic reconnection. *Physics of Plasmas (1994-present)*, *18*(3), 032309. doi: 10.1063/1.3568828

Buneman, O., Neubert, T., & Nishikawa, K.-I. (1992). Solar wind-magnetosphere interaction as simulated by a 3-d em particle code. *IEEE transactions on plasma science*, *20*(6), 810–816.
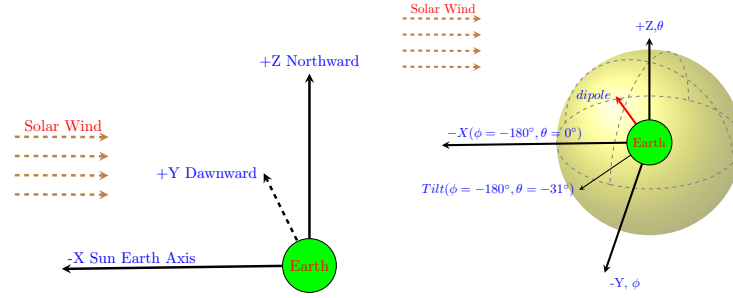
Cai, D., Esmaeili, A., Lembège, B., & Nishikawa, K.-I. (2015). Cusp dynamics under northward imf using three-dimensional global particle-in-cell simulations. *Journal of Geophysical Research: Space Physics*, *120*(10), 8368–8386.

Cai, D., Li, Y., Nishikawa, K.-I., Xiao, C., Yan, X., & Pu, Z. (2003). Parallel 3-D Electromagnetic Particle Code Using High Performance FORTRAN: Parallel TRISTAN. In *Space Plasma Simulation* (Vol. 615, pp. 25–53). Springer Berlin Heidelberg. doi: 10.1007/3-540-36530-3_2

Chang, Q., Xu, X., Xu, Q., Zhong, J., Xu, J., Wang, J., & Zhang, T. (2019). Multiple-point modeling the parker spiral configuration of the solar wind magnetic field at the solar maximum of solar cycle 24. *The Astrophysical Journal*, *884*(2), 102.

Cohen, O., Ma, Y., Drake, J. J., Glocer, A., Garraffo, C., Bell, J. M., & Gombosi, T. I. (2015, jun). THE INTERACTION OF VENUS-LIKE, m-DWARF PLANETS WITH THE STELLAR WIND OF THEIR HOST STAR. *The Astrophysical Journal*, *806*(1), 41. Retrieved from `https://doi.org/10.1088/0004-637x/806/1/41` doi: 10.1088/0004-637x/806/1/41

Cohen, O., Moschou, S.-P., Glocer, A., Sokolov, I. V., Mazeh, T., Drake, J. J., … Alvarado-Gómez, J. D. (2018, oct). Exoplanet modulation of stellar coronal radio emission. *The Astronomical Journal*, *156*(5), 202. Retrieved from `https://doi.org/10.3847/1538-3881/aae1f2` doi: 10.3847/1538-3881/aae1f2

Dimmock, A., Nykyri, K., Osmane, A., Karimabadi, H., & Pulkkinen, T. (2017). Dawn-dusk asymmetries of the earth's dayside magnetosheath in the magnetosheath interplanetary medium reference frame. *Dawn-Dusk Asymmetries in Planetary Plasma Environments*, 49–72.

Dimmock, A. P., Nykyri, K., Karimabadi, H., Osmane, A., & Pulkkinen, T. I. (2015, April). A statistical study into the spatial distribution and dawn-dusk asymmetry of dayside magnetosheath ion temperatures as a function of upstream solar wind conditions. *Journal of Geophysical Research (Space Physics)*, *120*(4), 2767-2782. doi: 10.1002/2014JA020734

Dimmock, A. P., Nykyri, K., & Pulkkinen, T. I. (2014, August). A statistical study of magnetic field fluctuations in the dayside magnetosheath and their dependence on upstream solar wind conditions. *Journal of Geophysical Research (Space Physics)*, *119*(8), 6231-6248. doi: 10.1002/2014JA020009

Dušík, Š., Granko, G., Šafránková, J., Němeček, Z., & Jelínek, K. (2010). Imf cone angle control of the magnetopause location: Statistical study. *Geophysical Research Letters*, *37*(19).

Eastwood, J. P. (2008). The science of space weather. *Philosophical Transactions of the Royal Society A: Mathematical, Physical and Engineering Sciences*, *366*(1884), 4489–4500.

Fairfield, D., Baumjohann, W., Paschmann, G., Lühr, H., & Sibeck, D. (1990). Upstream pressure variations associated with the bow shock and their effects on the magnetosphere. *Journal of Geophysical Research: Space Physics*, *95*(A4), 3773–3786.

Garcia, K., & Hughes, W. (2007). Finding the lyon-fedder-mobarry magnetopause: A statistical perspective. *Journal of Geophysical Research: Space Physics*, *112*(A6).

Gingell, P. W., Burgess, D., & Matteini, L. (2015, March). The Three-dimensional Evolution of Ion-scale Current Sheets: Tearing and Drift-kink Instabilities in the Presence of Proton Temperature Anisotropy. *The Astrophysical Journal*, *802*(1), 4. doi: 10.1088/0004-637X/802/1/4

Greenstadt, E. W., Green, I. M., Inouye, G. T., Hundhausen, A. J., Bame, S. J., & Strong, I. B. (1968, January). Correlated magnetic field and plasma observations of the Earth's bow shock. *\textbackslashjgr*, *73*, 51. doi: 10.1029/JA073i001p00051

Grygorov, K., Šafránková, J., Němeček, Z., Pi, G., Přech, L., & Urbář, J. (2017). Shape of the equatorial magnetopause affected by the radial interplanetary magnetic field. *Planetary and Space Science*, *148*, 28–34.

Haaland, S., Lybekk, B., Maes, L., Laundal, K., Pedersen, A., Tenfjord, P., … Snekvik, K. (2017). North-south asymmetries in cold plasma density in the magnetotail lobes:

Cluster observations. *Journal of Geophysical Research: Space Physics*, *122*(1), 136–149.

Haaland, S., Reistad, J., Tenfjord, P., Gjerloev, J., Maes, L., DeKeyser, J., … Dorville, N. (2014). Characteristics of the flank magnetopause: Cluster observations. *Journal of Geophysical Research: Space Physics*, *119*(11), 9019–9037.

Haaland, S., Runov, A., Artemyev, A., & Angelopoulos, V. (2019). Characteristics of the flank magnetopause: Themis observations. *Journal of Geophysical Research: Space Physics*, *124*(5), 3421–3435.

Heikkila, W. J. (2011). *Earth's Magnetosphere: Formed by the Low-latitude Boundary Layer*. Elsevier.

Jacobsen, K. S., Phan, T. D., Eastwood, J. P., Sibeck, D. G., Moen, J. I., Angelopoulos, V., … Fornaçon, K.-H. (2009). THEMIS observations of extreme magnetopause motion caused by a hot flow anomaly. *Journal of Geophysical Research (Space Physics)*, *114*, 8210. Retrieved from http://adsabs.harvard.edu/abs/2009JGRA..114.8210J

Jelínek, K., Němeček, Z., Šafránková, J., Shue, J.-H., Suvorova, A. V., & Sibeck, D. G. (2010). Thin magnetosheath as a consequence of the magnetopause deformation: THEMIS observations. *Journal of Geophysical Research (Space Physics)*, *115*, 10203. Retrieved from http://adsabs.harvard.edu/abs/2010JGRA..11510203J

Johnson, J. R., Wing, S., & Delamere, P. A. (2014). Kelvin helmholtz instability in planetary magnetospheres. *Space Science Reviews*, *184*(1-4), 1–31.

Karimabadi, H., Krauss-Varban, D., Huba, J., & Vu, H. (2004). On magnetic reconnection regimes and associated three-dimensional asymmetries: Hybrid, hall-less hybrid, and hall-mhd simulations. *Journal of Geophysical Research: Space Physics*, *109*(A9).

Karimabadi, H., Roytershteyn, V., Vu, H. X., Omelchenko, Y. A., Scudder, J., Daughton, W., … Geveci, B. (2014). The link between shocks, turbulence, and magnetic reconnection in collisionless plasmas. *Physics of Plasmas*, *21*, 062308. doi: 10.1063/1.4882875

Lavraud, B., Borovsky, J. E., Génot, V., Schwartz, S. J., Birn, J., Fazakerley, A. N., … Wild, J. A. (2009). Tracing solar wind plasma entry into the magnetosphere using ion-to-electron temperature ratio. *Geophys. Res. Lett.*, *36*, 18109. Retrieved from http://adsabs.harvard.edu/abs/2009GeoRL..3618109L

Le Contel, O., Retinò, A., Breuillard, H., Mirioni, L., Robert, P., Chasapis, A., … Saito, Y. (2016, June). Whistler mode waves and Hall fields detected by MMS during a dayside magnetopause crossing. *Geophysical Research Letters*, *43*(12), 5943-5952. doi: 10.1002/2016GL068968

Lindman, E. (1975). "Free-space" boundary conditions for the time dependent wave equation. *J. Comput. Phys.*, *18*(1), 66–78.

Liu, Y.-H., Li, T., Hesse, M., Sun, W., Liu, J., Burch, J., … Huang, K. (2019). Three-dimensional magnetic reconnection with a spatially confined x-line extent: Implications for dipolarizing flux bundles and the dawn-dusk asymmetry. *Journal of Geophysical Research: Space Physics*, *124*(4), 2819–2830.

Lu, J., Wang, M., Kabin, K., Zhao, J., Liu, Z.-Q., Zhao, M., & Li, G. (2015). Pressure balance across the magnetopause: Global mhd results. *Planetary and Space Science*, *106*, 108–115.

Lu, S., Lin, Y., Angelopoulos, V., Artemyev, A., Pritchett, P., Lu, Q., & Wang, X. (2016). Hall effect control of magnetotail dawn-dusk asymmetry: A three-dimensional global hybrid simulation. *Journal of Geophysical Research: Space Physics*, *121*(12), 11–882.

Luo, H., Chen, G., Du, A., & Xu, W. (2013). Solar wind dependence of energy coupling between solar wind and magnetosphere during intense northward imfs. *Planetary and Space Science*, *79*, 82–89.

Masters, A., Slavin, J., DiBraccio, G., Sundberg, T., Winslow, R., Johnson, C., … Korth, H. (2013). A comparison of magnetic overshoots at the bow shocks of mercury and saturn. *Journal of Geophysical Research: Space Physics*, *118*(7), 4381–4390.

Merka, J., Szabo, A., Šafránková, J., & Němeček, Z. (2003). Earth's bow shock and magnetopause in the case of a field-aligned upstream flow: Observation and model comparison. *Journal of Geophysical Research: Space Physics (1978–2012)*, *108*(A7),

976   –.

977 Němeček, Z., Šafránková, J., Zastenker, G. N., Pišoft, P., & Jelínek, K. (2002, April).
978   Low-frequency variations of the ion flux in the magnetosheath. *Planetary and Space*
979   *Science*, *50*(5-6), 567-575. doi: 10.1016/S0032-0633(02)00036-3

980 Omidi, N., Blanco-Cano, X., Russell, C. T., & Karimabadi, H. (2004, January). Dipolar
981   magnetospheres and their characterization as a function of magnetic moment. *Ad-*
982   *vances in Space Research*, *33*, 1996–2003. doi: 10.1016/j.asr.2003.08.041

983 Østgaard, N., Mende, S., Frey, H., Frank, L., & Sigwarth, J. (2003). Observations of
984   non-conjugate theta aurora. *Geophysical Research Letters*, *30*(21).

985 Palmroth, M., Ganse, U., Pfau-Kempf, Y., Battarbee, M., Turc, L., Brito, T., … von Alfthan,
986   S. (2018, August). Vlasov methods in space physics and astrophysics. *Living Reviews*
987   *in Computational Astrophysics*, *4*(1), 1. doi: 10.1007/s41115-018-0003-2

988 Paral, J., & Rankin, R. (2013). Dawn–dusk asymmetry in the kelvin–helmholtz instability
989   at mercury. *Nature Communications*, *4*(1), 1–5.

990 Park, J.-S., Shue, J.-H., Kim, K.-H., Pi, G., Němeček, Z., & Å afránková, J. (2016, July).
991   Global expansion of the dayside magnetopause for long-duration radial IMF events:
992   Statistical study on GOES observations. *Journal of Geophysical Research (Space*
993   *Physics)*, *121*(7), 6480–6492. doi: 10.1002/2016JA022772

994 Parks, G. K. (1991). Physics of space plasmas-an introduction. *Redwood City, CA, Addison-*
995   *Wesley Publishing Co., 1991, 547 p.*.

996 Paschmann, G., Sckopke, N., Papamastorakis, I., Asbridge, J., Bame, S., & Gosling, J.
997   (1981). Characteristics of reflected and diffuse ions upstream from the earth's bow
998   shock. *Journal of Geophysical Research: Space Physics (1978–2012)*, *86*(A6), 4355–
999   4364.

1000 Paularena, K., Richardson, J., Kolpak, M., Jackson, C., & Siscoe, G. (2001). A dawn-dusk
1001   density asymmetry in earth's magnetosheath. *Journal of Geophysical Research: Space*
1002   *Physics*, *106*(A11), 25377–25394.

1003 Pi, G., Němeček, Z., Šafránková, J., Grygorov, K., & Shue, J.-H. (2018). Formation of
1004   the dayside magnetopause and its boundary layers under the radial imf. *Journal of*
1005   *Geophysical Research: Space Physics*, *123*(5), 3533–3547.

1006 Samsonov, A. (2006, January). Numerical modelling of the Earth's magnetosheath for
1007   different IMF orientations. *Advances in Space Research*, *38*(8), 1652-1656. doi: 10
1008   .1016/j.asr.2005.06.009

1009 Samsonov, A. A. (2011, January). Propagation of inclined interplanetary shock through
1010   the magnetosheath. *Journal of Atmospheric and Solar-Terrestrial Physics*, *73*, 30–39.
1011   doi: 10.1016/j.jastp.2009.10.014

1012 Samsonov, A. A., Bogdanova, Y. V., Branduardi-Raymont, G., Sibeck, D. G., & Toth, G.
1013   (2020). Is the Relation Between the Solar Wind Dynamic Pressure and the Mag-
1014   netopause Standoff Distance so Straightforward? *Geophys. Res. Lett.*, *47*(8). doi:
1015   10.1029/2019GL086474

1016 Samsonov, A. A., Němeček, Z., Šafránková, J., & Jelínek, K. (2012, May). Why does the
1017   subsolar magnetopause move sunward for radial interplanetary magnetic field? *Jour-*
1018   *nal of Geophysical Research (Space Physics)*, *117*, 5221. doi: 10.1029/2011JA017429

1019 Samsonov, A. A., Sibeck, D. G., Å afránková, J., Němeček, Z., & Shue, J. H. (2017,
1020   March). A method to predict magnetopause expansion in radial IMF events by MHD
1021   simulations. *Journal of Geophysical Research (Space Physics)*, *122*(3), 3110-3126. doi:
1022   10.1002/2016JA023301

1023 Shue, J. H., Chao, J. K., Fu, H. C., Russell, C. T., Song, P., Khurana, K. K., & Singer,
1024   H. J. (1997, May). A new functional form to study the solar wind control of the mag-
1025   netopause size and shape. *Journal of Geophysical Research (Space Physics)*, *102*(A5),
1026   9497-9512. doi: 10.1029/97JA00196

1027 Shue, J.-H., Chao, J.-K., Song, P., McFadden, J., Suvorova, A., Angelopoulos, V., …
1028   Plaschke, F. (2009). Anomalous magnetosheath flows and distorted subsolar mag-
1029   netopause for radial interplanetary magnetic fields. *Geophysical Research Letters*,
1030   *36*(18).

Sibeck, D. G., Allen, R., Aryan, H., Bodewits, D., Brandt, P., Branduardi-Raymont, G., … others (2018). Imaging plasma density structures in the soft x-rays generated by solar wind charge exchange with neutrals. *Space Science Reviews*, *214*(4), 79.

Sibeck, D. G., Decker, R. B., Mitchell, D. G., Lazarus, A. J., Lepping, R. P., & Szabo, A. (2001). Solar wind preconditioning in the flank foreshock: IMP 8 observations. *J. Geophys. Res.*, *106*, 21675–21688. Retrieved from `http://adsabs.harvard.edu/abs/2001JGR...10621675S`

Sorathia, K., Merkin, V., Ukhorskiy, A., Allen, R., Nykyri, K., & Wing, S. (2019). Solar wind ion entry into the magnetosphere during northward imf. *Journal of Geophysical Research: Space Physics*, *124*(7), 5461–5481.

Spreiter, J. R., & Alksne, A. Y. (1969). Plasma flow around the magnetosphere. *Reviews of Geophysics*, *7*(1-2), 11–50.

Suvorova, A., & Dmitriev, A. (2015). Magnetopause inflation under radial imf: Comparison of models. *Earth and Space Science*, *2*(4), 107–114.

Suvorova, A. V., Shue, J. H., Dmitriev, A. V., Sibeck, D. G., McFadden, J. P., Hasegawa, H., … Němeček, Z. (2010, October). Magnetopause expansions for quasi-radial interplanetary magnetic field: THEMIS and Geotail observations. *Journal of Geophysical Research (Space Physics)*, *115*(A10), A10216. doi: 10.1029/2010JA015404

Tan, B., Lin, Y., Perez, J., & Wang, X. (2011). Global-scale hybrid simulation of dayside magnetic reconnection under southward imf: Structure and evolution of reconnection. *Journal of Geophysical Research: Space Physics*, *116*(A2).

Trattner, K., Mulcock, J., Petrinec, S., & Fuselier, S. (2007). Location of the reconnection line at the magnetopause during southward imf conditions. *Geophysical Research Letters*, *34*(3).

Treumann, R. A., & Baumjohann, W. (2013). Collisionless magnetic reconnection in space plasmas. *Frontiers in Physics*, *1*, 31.

Tsurutani, B. T., & Lakhina, G. S. (1997). Some basic concepts of wave-particle interactions in collisionless plasmas. *Reviews of Geophysics*, *35*(4), 491–501.

Turc, L., Tarvus, V., Dimmock, A., Battarbee, M., Ganse, U., Johlander, A., … Palmroth, M. (2020). Asymmetries in the earth's dayside magnetosheath: results from global hybrid-vlasov simulations. *Annales Geophysicae Discussions*, *2020*, 1–24. Retrieved from `https://www.ann-geophys-discuss.net/angeo-2020-13/` doi: 10.5194/angeo-2020-13

Turner, D., Wilson, L., Liu, T., Cohen, I., Schwartz, S., Osmane, A., … others (2018). Autogenous and efficient acceleration of energetic ions upstream of earth's bow shock. *Nature*, *561*(7722), 206–210.

Villasenor, J., & Buneman, O. (1992). Rigorous charge conservation for local electromagnetic field solvers. *Comput. Phys. Commun.*, *69*(2), 306–316.

Šafránková, J., Němeček, Z., Santolík, O., Sibeck, D. G., Zastenker, G. N., & Skalsky, A. (2000). The Flank Magnetopause: Interball Observations. *Advances in Space Research*, *25*, 1503–1510. Retrieved from `http://adsabs.harvard.edu/abs/2000AdSpR..25.1503S`

Walsh, A. P., Haaland, S., Forsyth, C., Keesee, A. M., Kissinger, J., Li, K., … Taylor, M. G. G. T. (2014, July). Dawn-dusk asymmetries in the coupled solar wind-magnetosphere-ionosphere system: a review. *Annales Geophysicae*, *32*, 705–737. Retrieved from `https://ui.adsabs.harvard.edu/abs/2014AnGeo..32..705W` doi: 10.5194/angeo-32-705-2014

Walsh, B. M. (2017). Magnetopause plasma parameters and asymmetries in solar wind–magnetosphere coupling. *Dawn-Dusk Asymmetries in Planetary Plasma Environments*, 29–39.

Walsh, B. M., Sibeck, D. G., Wang, Y., & Fairfield, D. H. (2012, December). Dawn-dusk asymmetries in the Earth's magnetosheath. *Journal of Geophysical Research (Space Physics)*, *117*(A12), A12211. doi: 10.1029/2012JA018240

Wang, C.-P., Lyons, L. R., Weygand, J. M., Nagai, T., & McEntire, R. W. (2006). Equatorial distributions of the plasma sheet ions, their electric and magnetic drifts, and

magnetic fields under different interplanetary magnetic field bz conditions. *Journal of Geophysical Research: Space Physics*, *111*(A4).

Wang, J., Guo, Z., Ge, Y. S., Du, A., Huang, C., & Qin, P. (2018, October). The responses of the earth's magnetopause and bow shock to the IMF B_z and the solar wind dynamic pressure: a parametric study using the AMR-CESE-MHD model. *Journal of Space Weather and Space Climate*, *8*, A41. doi: 10.1051/swsc/2018030

Wang, Y.-M., Grappin, R., Robbrecht, E., & Sheeley Jr, N. (2012). *The Astrophysical Journal*, *749*(2), 182.

Willis, D. (1978). The magnetopause: Microstructure and interaction with magnetospheric plasma. *Journal of Atmospheric and Terrestrial Physics*, *40*(3), 301–322.

Wing, S., Johnson, J. R., Chaston, C. C., Echim, M., Escoubet, C. P., Lavraud, B., … Wang, C. P. (2014, November). Review of Solar Wind Entry into and Transport Within the Plasma Sheet. *Space Science Reviews*, *184*(1-4), 33-86. doi: 10.1007/ s11214-014-0108-9

Yu, Y., & Ridley, A. J. (2009, December). The response of the magnetosphere-ionosphere system to a sudden dynamic pressure enhancement under southward IMF conditions. *Annales Geophysicae*, *27*(12), 4391-4407. doi: 10.5194/angeo-27-4391-2009

Zhang, H., Fu, S., Pu, Z., Lu, J., Zhong, J., Zhu, C., … Liu, L. (2019, aug). Statistics on the magnetosheath properties related to magnetopause magnetic reconnection. *The Astrophysical Journal*, *880*(2), 122. Retrieved from `https://doi.org/ 10.3847%2F1538-4357%2Fab290e` doi: 10.3847/1538-4357/ab290e

Solar Wind

+Z Northward

Solar Wind

+Y Dawnward

-X Sun Earth Axis

Earth

$+Z, \theta$

$dipole$

$-X(\phi = -180°, \theta = 0°)$

Earth

$Tilt(\phi = -180°, \theta = -31°)$

$-Y, \phi$

1

**Figure 1.** Code coordinates scheme (left) and spherical coordinates illustration used in MP derivation (right)
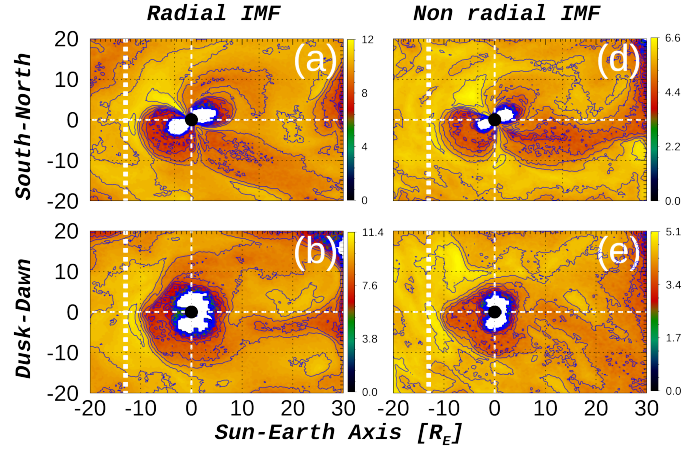
Figure 2. Solar wind 2D density contours in the XZ (Y=0), XY (Z=0), and YZ (X=0) planes for both IMF orientations. Vertical dashed lines at $X = -13R_E$ indicate the position of linear density profiles shown in Fig. 8. Panels (a), (b), and (c) are for radial IMF and panels (d), (e), and (f) are for non-radial IMF
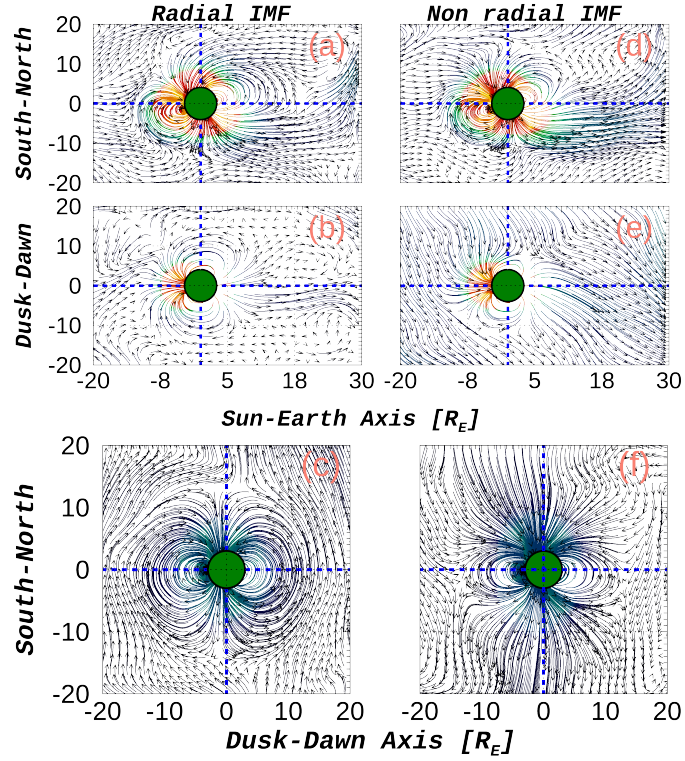
Figure 3. Fields 2D topology in the XZ (Y=0), XY (Z=0), and YZ (X=0) planes for both IMF orientations. Panels (a), (b), and (c) are for radial IMF and panels (d), (e), and (f) are for non radial IMF
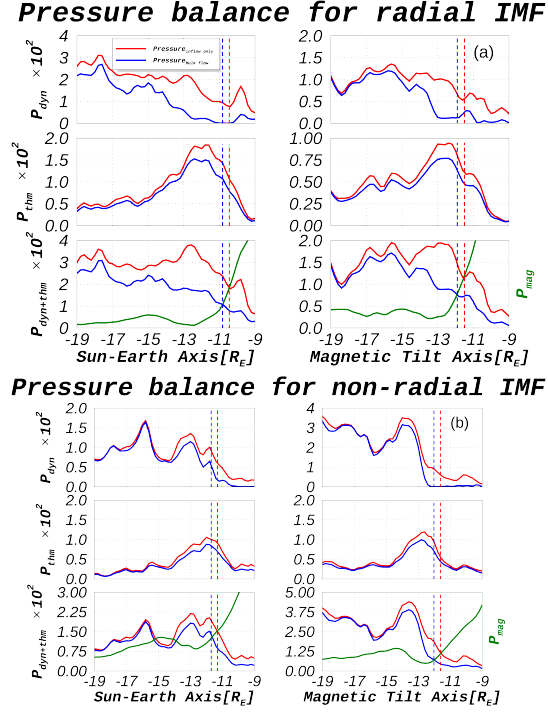
Figure 4. MP size derivation from pressure balance system measured radially at two locations. The MP is derived along the Earth-Sun axis (OX) and along the tilted magnetic equatorial axis. Bulk flow (blue) and inflow (red) pressures show different MP locations. For radial IMF, panel (a), it is found that MP=[-10.8, -10.5]R_E derived with bulk and inflow pressures only along Sun-Earth Axis and MP=[-11.9,-11.5]R_E along the tilted magnetic equatorial axis. Respectively for non-radial IMF, panel(b), MP=[-11.7,-11.3] and [-12., -11.6]R_E.
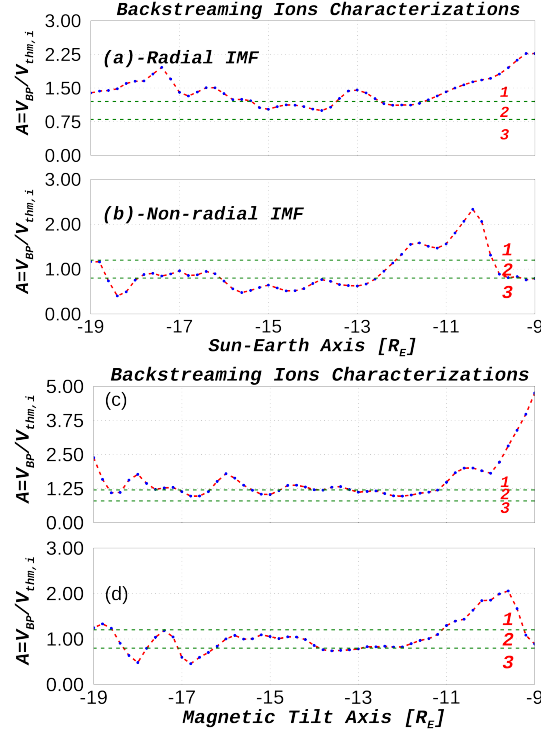
1

Figure 5. Characterization of backstreaming ions in the dayside magnetosphere based on their bulk flow ratio on thermal speed (Adopted from (Bonifazi & Moreno, 1981b)). Panels, a and b are taken along OX-axis in XZ plane and panels c, and d are taken along tilted magnetic equatorial axis for both IMF orientations. This figure shows the reflected and diffuse fractions of the backstreaming ions (their respective percentages are shown in table 5). Scaling factor "A" is used for the characterization of backstreaming ions. A>1.2 denotes reflected ions(region-1) in the plots. A<0.8 denotes diffuse ions(region-3). 0.8<A<1.2 denotes intermediate ions(region-2)
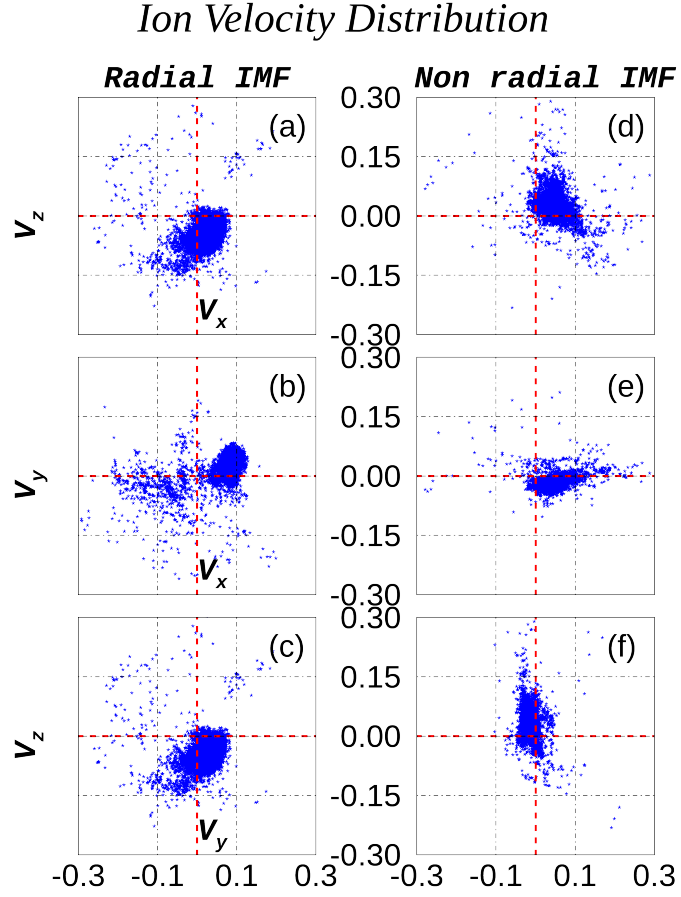
Figure 6. Ion Velocity dayside distribution measured from $-20R_E$ to the planet position (z=y=0) along Sun-Earth axis. Left panels are for radial IMF and right panels are for non radial IMF orientation.
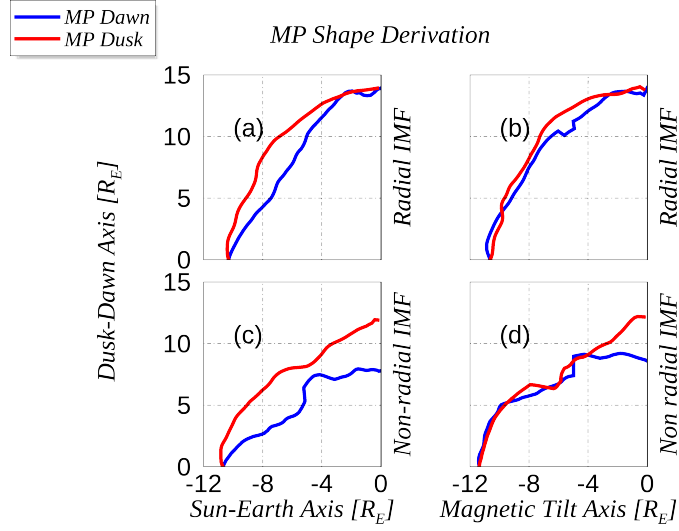
1

Figure 7. Panels (a) and (b) show the MP shape for radial IMF along Sun-Earth and tilted magnetic equatorial axis. Similarly, panels (c) and (d) are the same but for non-radial IMF. We remark that the size shown here is approximately equivalent to the MP sizes derived from the density steepening.
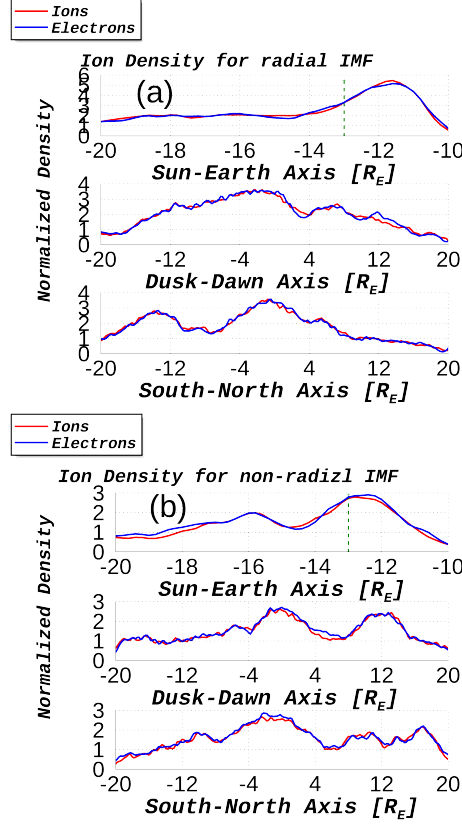
Figure 8. Ion and electron densities are plotted in three directions, along OX (Y=Z=0), OY (X=-13, and Z=0), and OZ (X=-13, and Y=0)), just outside the MP for radial IMF in panel a and for non-radial IMF in panel b. Their values are normalized to the initial densities. The density profile is plotted only in the dayside region as shown with vertical dashed lines (at $X = -13R_E$) in Fig. 2. This figure also shows the plasma quasi neutrality.
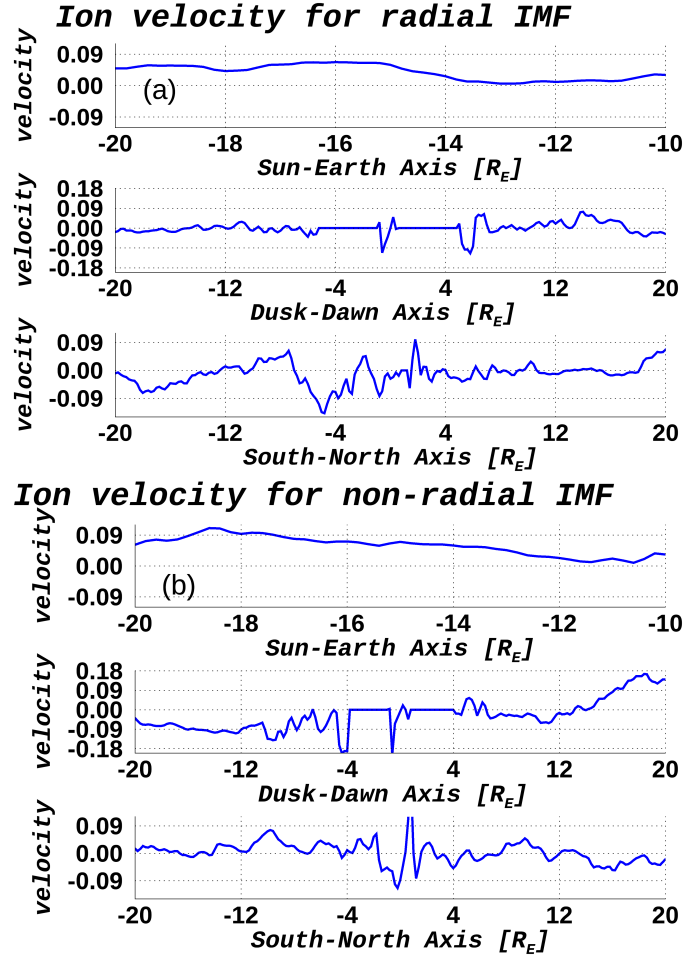
Figure 9. Bulk ion velocity modulus for both IMF orientations are plotted along three directions as in Fig. 8.
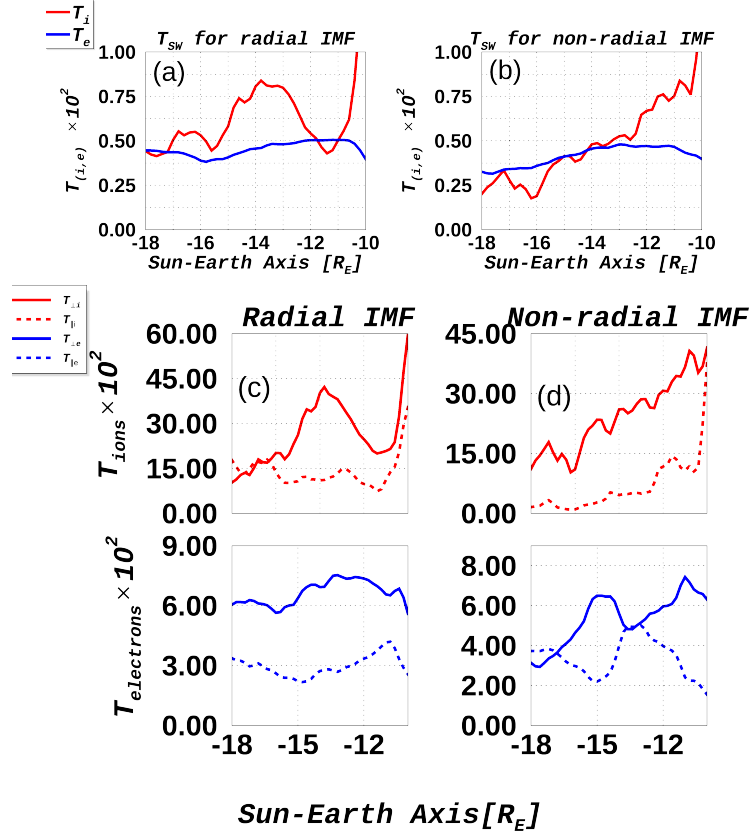
Figure 10. Ion and electron temperatures are shown in the dayside magnetosphere for both IMF orientations(panels a and b). The average ion to electron temperature ratios in the magnetosheath between -14 and -12.5R_E are $< T_i/T_e >= 1.72$ and $< T_i/T_e >= 1.1$ for radial (panel a) and non-radial IMF (panel b), respectively. Temperature anisotropy for ions and electrons for both IMF orientations are shown in panel c and d. The $T_{\perp i}/T_{\parallel i}$, and $T_{\perp e}/T_{\parallel e}$ ratios averaged between -18 to -10R_E are (2,2.3) respectively for radial IMF. This ratio reads (6,1.8) for non-radial IMF.
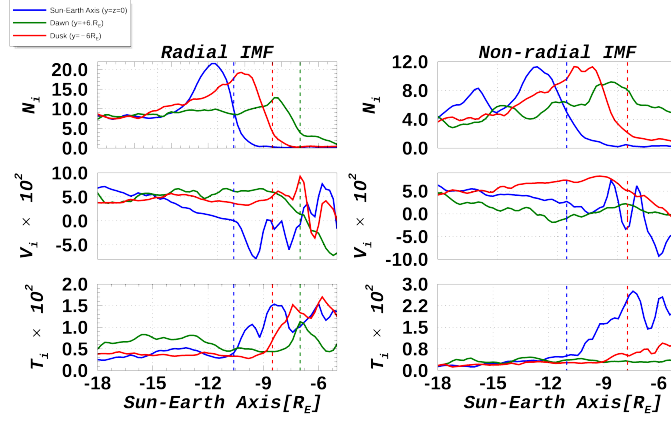
Figure 11. Ion density, velocity, and temperature (N_i, V_i, T_i) are plotted along the OX-axis and at ± 6 on both dusk and dawn directions in the XY plane. Vertical dashed lines show the MP position at the subsolar point(blue), dusk flank(red), and dawn flank(green) quantities show dusk-dawn asymmetry at the $\pm 6 R_E$.
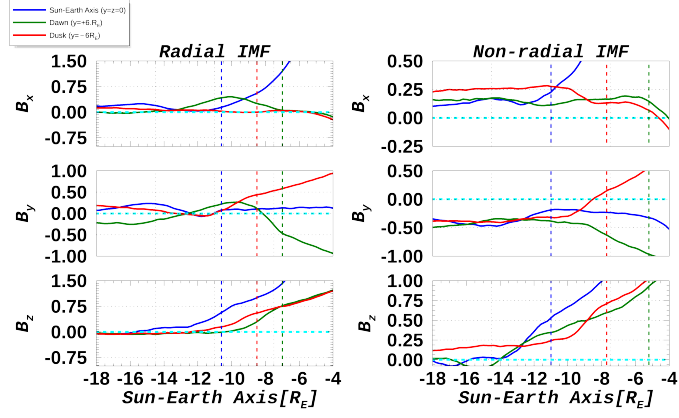
1

Figure 12. IMF components, B_x, B_y, and B_z are plotted along the OX-axis and at ± 6 on both dawn and dusk directions in the XY plane. Vertical dashed lines show the MP position at the subsolar point (blue), dusk flank (red), and dawn flank (green) quantities show dusk-dawn asymmetry at the $\pm 6 R_E$. Horizontal cyan dashed line shows the zero value of IMF. Change of IMF polarity is significantly seen in B_y component.